1. Paper 1 to-do list

1. Make a photometry table - one from the hand-extracted, one from dendrogram-extracted? Section 4.3
2. Is any discussion of the gas kinematics warranted? That should perhaps be relegated to the (lack of?) disks paper
3. create Table reftab:linelist = **??** (Section 4.4)
4. Show a 'core' mass histogram in Section 4.4
5. Repeat Section 4.5.1 for e8 and north
6. move Section 4.8.2 to discussion

2. Introduction

We introduce...

3. Observations

As part of ALMA Cycle 2 program 2013.1.00308.S, we observed a $\sim 2' \times 1'$ region centered between W51 IRS2 and W51 e1/e2 with a 37-pointing mosaic. Two configurations of the 12m array were used, achieving a resolution of $0.2''$. Additionally, a 12-pointing mosaic was performed using the 7m array, hypothetically probing scales up to $\sim 28''$. The full UV coverage was from ~ 12 to ~ 1500 m (figure 1).

3.1. Data Reduction

Data reduction was performed using CASA. The QA2-produced data products were combined using the standard inverse variance weighting. Two sets of images were produced for different aspects of the analysis, one including the 7m array data and one including only 12m data. Except where otherwise noted, the 12m-only data were used in order to focus on the compact structures.

3.1.1. Continuum

A continuum image combining all 4 spectral windows was produced using `tclean`. We phase self-calibrated the data on baselines longer than 100m to increase the dynamic range. The final image was cleaned with 50000 iterations to a threshold of 5 mJy. The lowest noise level in the image, away from bright sources, is ~ 0.2 mJy/beam, but near the bright sources e2 and IRS2, the noise reached as high as ~ 2 mJy/beam. Deeper cleaning was attempted, but lead to instabilities.

3.1.2. Lines

We produced spectral image cubes of the lines listed in Tables 2, 3, 4, and 5.

4. Results & Analysis

4.1. Source Identification

We used the `dendrogram` method described by **?** and implemented in `astrodendro` to identify sources. We used a minimum value of 1 mJy/beam ($\sim 5-\sigma$) and a minimum $\Delta = 0.4$ mJy/beam ($\sim 2-\sigma$) with minimum 10 pixels (each pixel is $0.05''$). This cataloging yielded over 8000 candidate sources, of which the majority are noise or artifacts around the brightest sources. To filter out these bad sources, we created a noise map taking the local RMS of the `tclean`-produced residual map over a $\sigma = 30$ pixel ($1.5''$) gaussian. We then removed all sources with peak S/N < 8, mean S/N per pixel < 5, and minimum S/N per pixel < 1. We also only included the smallest sources in the dendrogram, the "leaves". These parameters were tuned by checking against "real" sources identified by eye and selected using `ds9`: most real sources are recovered and few spurious sources (< 10) are included. The resulting catalog includes 113 sources.

The 'by-eye' core extraction approach, in which we placed ds9 regions on all sources that look 'real', produced a more reliable but less complete (and less quantifiable) catalog containing 75 sources. This catalog is more useful in the regions around the bright sources e2 and north, since these regions are affected by substantial uncleaned PSF sidelobe artifacts. In particular, the dendrogram catalog includes a number of sources around e2/e8 that, by eye, appear to be parts of continuous extended emission rather than local peaks; "streaking" artifacts in the reduced data result in their identification despite our threshold criteria. The dendrogram extraction also identified sources within the IRS 2 H II region that are not dust sources. Dendrogram extraction missed a few clear sources in the low-noise regions away from W51 Main and IRS 2 because the identification criteria were too conservative.

When extracting properties of the 'by-eye' sources, we used variable sized circular apertures, where the apertures were selected to include all of the detectable symmetric emission around a central peak up to a maximum radius $r \sim 0.6''$. This approach is necessary, as some of the sources are not centrally peaked and are therefore likely to be spatially resolved starless cores.

4.2. The spatial distribution of cores

The detected cores are not uniformly distributed across the observed region. The most notable feature in the spatial distribution is their alignment: most cores collect along approximately linear features. This is especially evident in W51 IRS2, where the core density is very high and there is virtually no deviation from the line. The e8 filament is also notably linear, though there area few sources detected just off the filament.

On a larger scale, the e8 filament points toward e2, apparently tracing a slightly longer filamentary structure. With some imagination, this might be extended along the entire northeast ridge to eventually connect in a broad half-circle with the IRS2 filament (Figure 2). This morphology hints at a possible sequential star formation event, where some central bubble has swept gas into these filaments. However, this ring has no counterparts in ionized gas, and there is little reason to expect such circular symmetry from a real cloud, so the star forming circle may be merely a figment.

Whether it is physical or not, there is a notable lack of cores within the circle. There is no lack of molecular gas, however, as both CO and H_2CO emission fill the full field of view.

4.3. Photometry

We created a catalog of the sources including their peak and mean flux density, their centroid, and their geometric

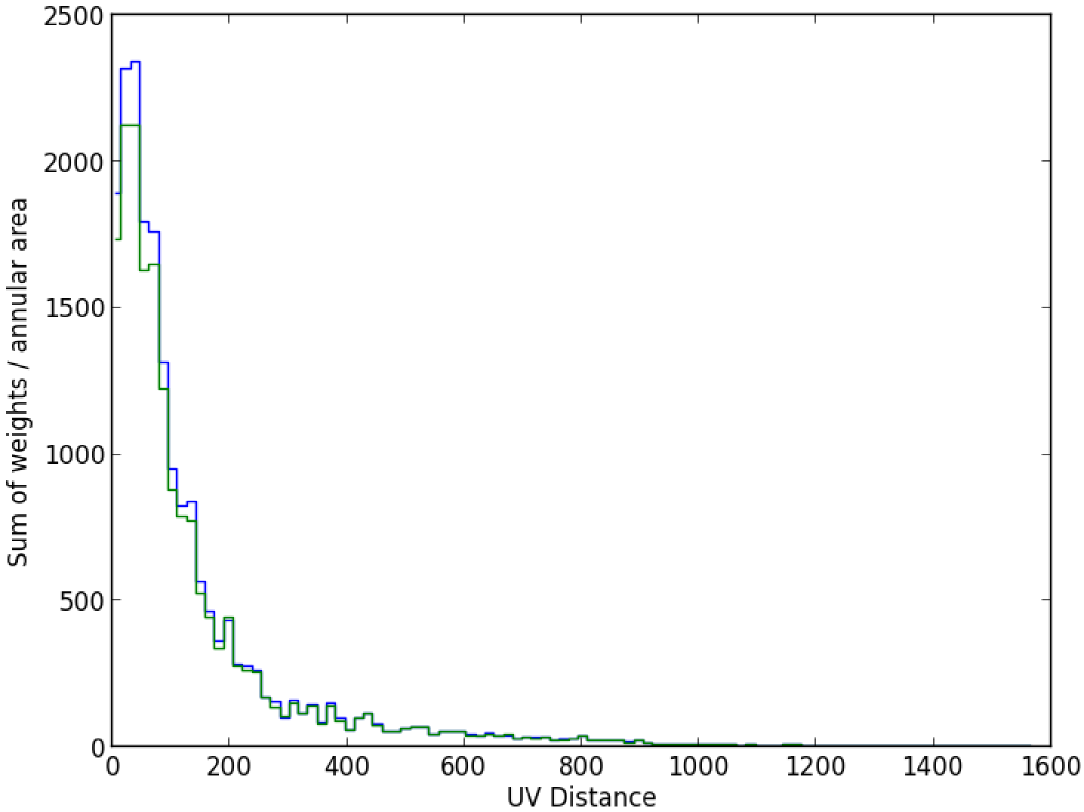

Fig. 1. A weighted histogram of the visibility weights as a function of UV distance; this approximately shows the amount of data received at each baseline length.

Table 1. Spectral Setup

SpwID	Minimum Frequency GHz	Maximum Frequency GHz	Channel Width kHz
0	218.11930228	218.619301	-122.07
1	218.36288652	220.355073	-488.281
2	230.376575	232.36876148	488.281
3	232.981075	234.97326148	488.281

properties. For each source, we further extracted aperture photometry around the centroid in 6 apertures: 0.2, 0.4, 0.6, 0.8, 1.0, and 1.5″. We performed the same aperture photometry on the W51 Ku-band images from **?** to estimate the free-free contribution to the observed flux density measurements. These measurements are reported in Table ....

The source flux density distribution is shown in Figure 4. The most common nearest-neighbor separation between cataloged cores is $\sim 0.3''$, which implies that the larger apertures double-count some pixels. The smallest separation is $0.26''$, so the $0.2''$ aperture contains only unique pixels.

Except where noted below, the hand-selected sources are used for further analysis as they are more reliable. However, to encourage reproducible results - which hand-extracted source positions defy - we also provide the algorithmically-extracted and selected dendrogram catalog.

4.3.1. Distribution Functions

We fit power law distributions to each aperture's flux distribution using the packages `plfit` and `PowerLaw` (https://github.com/keflavich/plfit, https://github.com/jeffalstott/powerlaw; **??**). The power-laws steepen slightly from $\alpha = 2.0 \pm 0.12$ to $\alpha = 2.2 \pm 0.16$ for larger apertures. The minimum flux density represented by a power law increases from $\sim$ 20 mJy for the peak flux density distribution to 0.4 Jy for the largest aperture (14-280 $M_\odot$ at 20K). These slopes are shallower than the Salpeter-like slope for the mass function derived by (**?**) for their sample, though with only modest significance ($< 3-\sigma$). Of course, these measurements are of the continuum flux density, not directly of the mass, and so a direct comparison may not be appropriate. We revisit this question after assessing the dust temperature in Section 4.4.

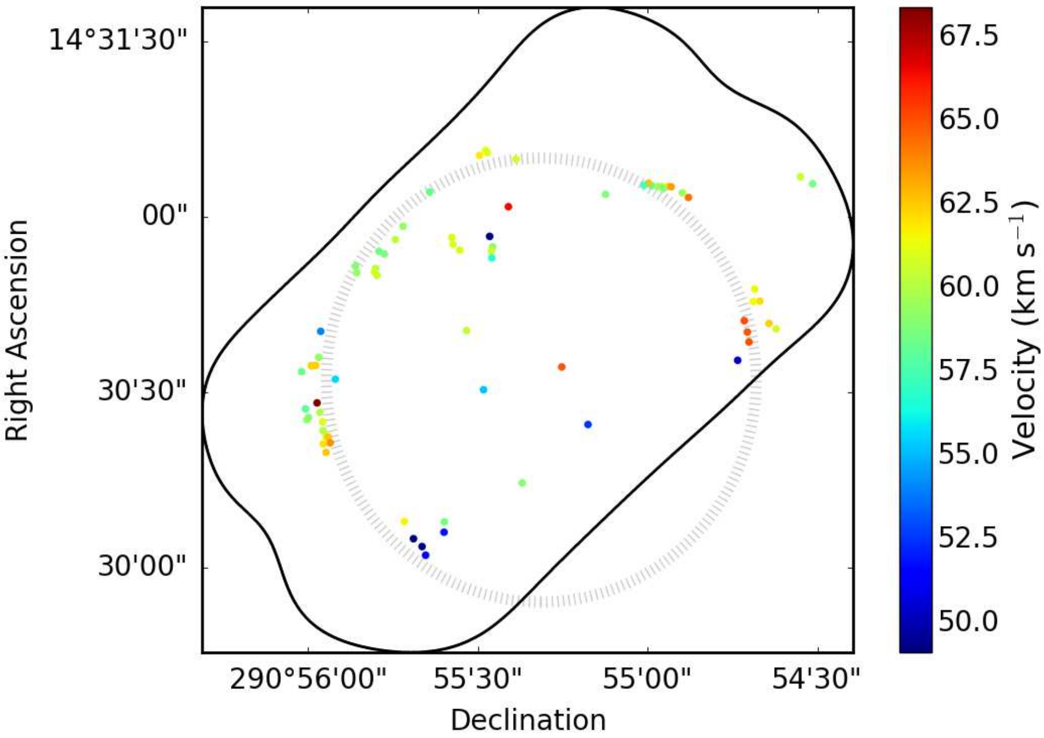

Fig. 2. The spatial distribution of the hand-identified core sample. The black outer contour shows the observed field of view. The dashed circle shows a hypothetical ring of star formation.

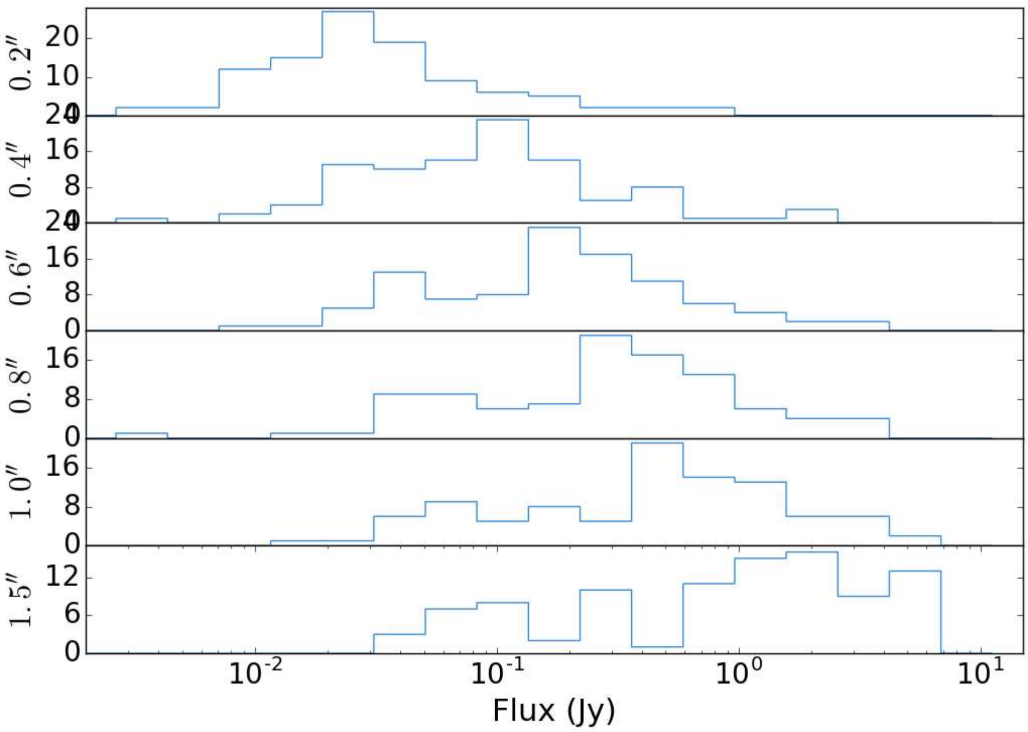

Fig. 3. Histograms of the core flux densities measured with circular apertures centered on the dendrogram-extracted core centroids. The aperture size is listed in the y-axis label. Free-free-dominated sources are excluded.

Table 2. Spectral Lines in SPW 0

Line Name	Frequency GHz
$H_2CO\ 3_{0,3} - 2_{0,2}$	218.22219
$H_2CO\ 3_{2,2} - 2_{2,1}$	218.47564
$CH_3OH\ 4_{2,2} - 3_{1,2}$	218.44005
$CH_3OCHO\ 17_{3,14} - 16_{3,13}E$	218.28083
$CH_3OCHO\ 17_{3,14} - 16_{3,13}A$	218.29787
$CH_3CH_2CN\ 24_{3,21} - 23_{3,20}$	218.39002
Acetone $8_{7,1} - 7_{4,4}$AE	218.24017
$O^{13}CS$ 18-17	218.19898
$CH_3OCH_3\ 23_{3,21} - 23_{2,22}AA$	218.49441
$CH_3OCH_3\ 23_{3,21} - 23_{2,22}EE$	218.49192
$CH_3NCO\ 25_{1,24} - 24_{1,23}$	218.5418
$CH_3SH\ 23_2 - 23_1$	218.18612

Table 3. Spectral Lines in SPW 1

Line Name	Frequency GHz
$H_2CO\ 3_{2,1} - 2_{2,0}$	218.76007
HC_3N 24-23	218.32471
HC_3Nv_7=1 24-23a	219.17358
HC_3Nv_7=1 24-23a	218.86063
HC_3Nv_7=2 24-23	219.67465
OCS 18-17	218.90336
SO $6_5 - 5_4$	219.94944
HNCO $10_{1,10} - 9_{1,9}$	218.98102
HNCO $10_{2,8} - 9_{2,7}$	219.73719
HNCO $10_{0,10} - 9_{0,9}$	219.79828
HNCO $10_{5,5} - 9_{5,4}$	219.39241
HNCO $10_{4,6} - 9_{4,5}$	219.54708
HNCO $10_{3,8} - 9_{3,7}$	219.65677
$CH_3OH\ 8_{0,8} - 7_{1,6}$	220.07849
$CH_3OH\ 25_{3,22} - 24_{4,20}$	219.98399
$CH_3OH\ 23_{5,19} - 22_{6,17}$	219.99394
$C^{18}O$ 2-1	219.56036
H_2CCO 11-10	220.17742
$HCOOH\ 4_{3,1} - 5_{2,4}$	219.09858
$CH_3OCHO\ 17_{4,13} - 16_{4,12}A$	220.19027
$CH_3CH_2CN\ 24_{2,22} - 23_{2,21}$	219.50559
Acetone $21_{1,20} - 20_{2,19}$AE	219.21993
Acetone $21_{1,20} - 20_{1,19}$EE	219.24214
Acetone $12_{9,4} - 11_{8,3}$EE	218.63385
$H_2{}^{13}CO\ 3_{1,2} - 2_{1,1}$	219.90849
$SO_2\ 22_{7,15} - 23_{6,18}$	219.27594
$SO_2\ v_2 = 1\ 20_{2,18} - 19_{3,17}$	218.99583
$SO_2\ v_2 = 1\ 22_{2,20} - 22_{1,21}$	219.46555
$SO_2\ v_2 = 1\ 16_{3,13} - 16_{2,14}$	220.16524

4.4. Temperature estimation of the continuum sources

The temperature is a critical ingredient for determining the total mass of each continuum source or region. Since we do not have any means of directly determining the dust temperature, as the SED peak is well into the THz regime and inaccessible with any existing instruments at the requisite resolution, we employ alternative indicators. Above a density $n \gtrsim 10^5 - 10^6$ cm^{-3}, the gas and dust become strongly collisionally coupled, meaning the gas temperature should accurately reflect the dust temperature. Below this density, the two may be decoupled.

The average dust temperature, as estimated from Herschel Hi-Gal SED fits (**??**), is 38 K when including the 70 μm data or 26 K when excluding it. This average is obtained over a $\sim 45''$ (~ 1 pc) beam and therefore is likely to be strongly biased toward the hottest dust in the HII regions and around the massive cores, which have temperatures reaching > 300 K (**?**). Despite these uncertainties, this bulk measurement provides us with a reasonable range to assume for the uncoupled, low-density dust, which (weakly) dominates the mass (see Section 4.7).

One constraint on the dust temperature we can employ is the absolute surface brightness. For some regions,

Table 4. Spectral Lines in SPW 2

Line Name	Frequency GHz
^{12}CO $2-1$	230.538
OCS 19-18	231.06099
HNCO $28_{1,28}-29_{0,29}$	231.873255
CH_3OH $10_{2,9}-9_{3,6}$	231.28115
^{13}CS 5-4	231.22069
NH_2CHO $11_{2,10}-10_{2,9}$	232.27363
H30α	231.90093
CH_3OCHO $12_{4,9}-11_{3,8}$E	231.01908
CH_3CH_2OH $5_{5,0}-5_{4,1}$	231.02517
CH_3OCH_3 $13_{0,13}-12_{1,12}$AA	231.98772
N_2D+ 3-2	231.32183
g-CH_3CH_2OH $13_{2,11}-12_{2,10}$	230.67255
g-CH_3CH_2OH $6_{5,1}-5_{4,1}$	230.79351
g-CH_3CH_2OH $16_{5,11}-16_{4,12}$	230.95379
g-CH_3CH_2OH $14_{0,14}-13_{1,13}$	230.99138
SO_2 $v_2=1$ $6_{4,2}-7_{3,5}$	232.21031
CH_3SH 16_2-16_1	231.75891
CH_3SH 7_3-8_2	230.64608

Table 5. Spectral Lines in SPW 3

Line Name	Frequency GHz
CH_3OH $4_{2,3}-5_{1,4}$	234.68345
CH_3OH $5_{-4,2}-6_{-4,3}$	234.69847
CH_3OH $18_{3,15}-17_{4,14}$	233.79575
$^{13}CH_3OH$ $5_{1,5}-4_{1,4}$	234.01158
PN $5-4$	234.93569
NH_2CHO $11_{5,6}-10_{5,5}$	233.59451
Acetone $12_{11,2}-11_{10,1}$AE	234.86136
SO_2 $16_{6,10}-17_{5,13}$	234.42159
CH_3NCO $27_{2,26}-26_{2,25}$	234.08812
CH_3SH 15_2-15_1	234.19145

especially the e8 filament and the hot cores, the surface brightness is substantially brighter than is possible for a beam-filling, optically thick blackbody at 20 K, providing a lower limit on the dust temperature ranging from 30 K (40 mJy/beam) to 600 K (1 Jy/beam). Toward most of this emission, optically-thick free-free emission can be strongly ruled out as the driving mechanism using existing data that limits the free-free contribution to be $<50\%$ if it is optically thick, and negligible ($<<1\%$) if it is optically thin at radio wavelengths (**??**).

To gain a more detailed measurement of the dust temperature in regions where it is likely to be coupled to the gas, we use the peak brightness temperature $T_{B,max}$ of spectral lines along the line of sight. If the observed molecule is in local thermal equilibrium, as is expected if the density is high enough to be collisionally coupled to the dust, and it is optically thick, the brightness temperature provides an approximate measurement of the local temperature near the $\tau=1$ surface. If any of these assumptions do not hold, $T_{B,max}$ will set a lower limit on the true gas temperature. Only nonthermal (maser) emission would push $T_{B,max}>T_{gas}$.

One potential problem with this approach is if the gas becomes optically thick before probing most of the dust. Some transitions of more abundant molecules, e.g., CO and H_2CO, are likely to be affected by this issue. However, many of the molecules included in the observations have lower abundances and are likely to be optically thin along most of the line of sight.

Some sources have no detected line emission aside from the molecular cloud species CO and H_2CO. The minimum density requirement imposed by a continuum detection at our limit of 1.6 mJy is $n>10^{7.5}$ cm^{-3} for a spherical source. At such high density, it is unlikely that the species are undetected because they are subthermally excited. More likely, the line-nondetection sources have an underyling emission source that is very compact, optically thick, and/or cold.

Figure 5 shows the distribution of peak line brightnesses for the continuum sources. The spectra used to determine this brightness are the mean spectra over the continuum photometry aperture. To obtain the peak line brightness, we fit Gaussian profiles to each identified line listed in Table **??**, rejecting those with poor fits. The line brightnesses reported in the figure are the sum of the continuum-subtracted peak line brightness and the continuum brightness. Excepting CO and H_2CO, which are excluded from the plot, CH_3OH is the brightest line toward most sources.

We use these peak line brightness temperatures to compute the 'corrected' masses of the continuum sources. For sources with $T_{B,max}<20$ K, we assume $T_{dust}=20$ K to

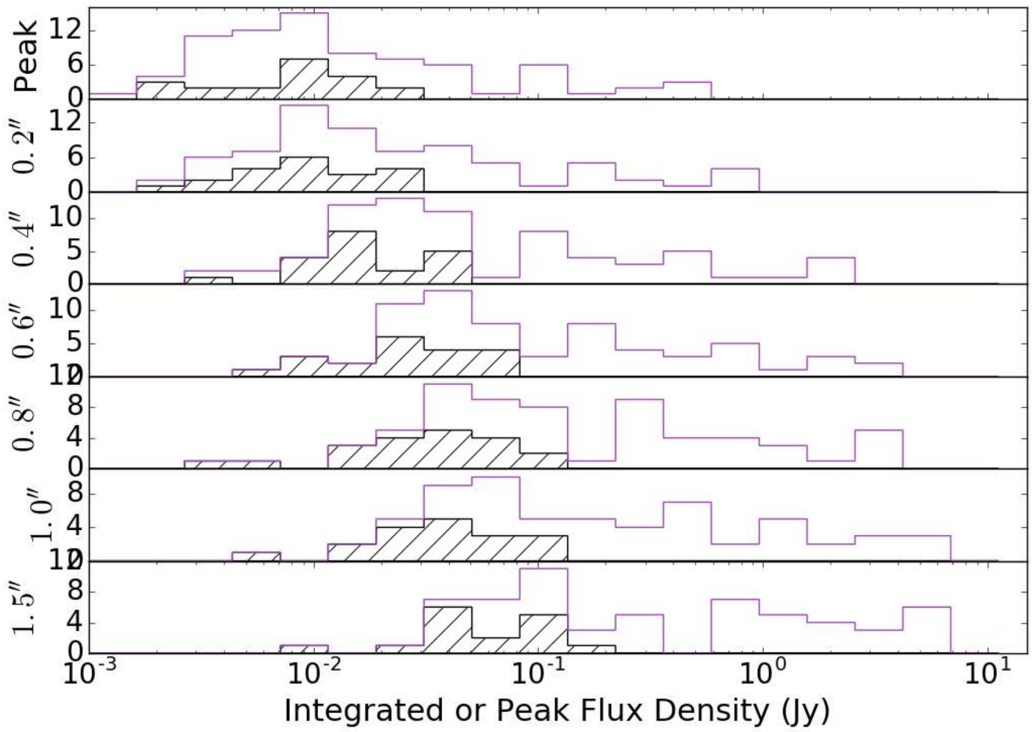

Fig. 4. Histograms of the core flux densities measured with circular apertures centered on the hand-extracted core positions. The aperture size is listed in the y-axis label. For the top plot, labeled 'Peak', this is the peak flux density in Jy/beam. For the rest, it is the integrated flux density in the specified aperture. The unfilled data show all sources and the hashed data are for starless core candidates (Section 4.5).

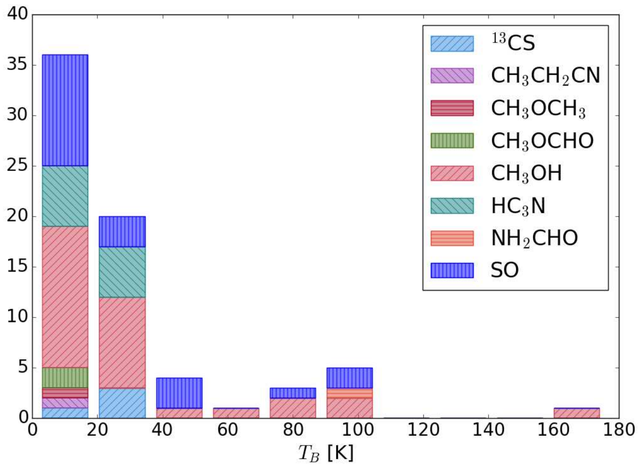

Fig. 5. Histogram of the brightest line toward each continuum source. The bars are colored by the molecular species associated with the brightest line that is not associated with extended molecular cloud emission, i.e., CO and its isotopologues and H_2CO are excluded.

avoid producing unreasonably high masses; in such sources the lines are likely to be optically thin and/or subthermally excited. The correction is illustrated in Figure 6.

4.5. The nature of the continuum sources

Millimeter continuum sources in star-forming regions are usually assumed to be either protostars or starless cores. However, in this high-mass star-forming region, we have to consider both those possibilities and potential free-free sources or high-luminosity main-sequence stars embedded in dust.

We fit each of up to ~ 50 lines (see Table ...) with Gaussian profiles to attempt to determine the relative line strengths toward each source. Most sources were detected in at least $\sim 5-10$ lines, though some of these are associated with interstellar rather than circumstellar material, i.e., H_2CO, CO, ^{13}CS. For sources with detections in non-

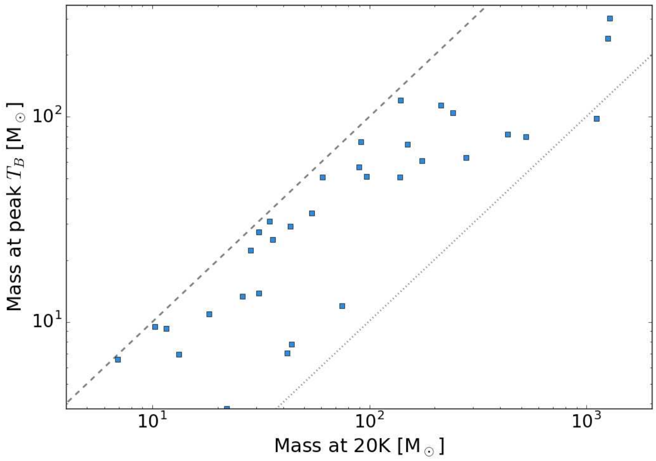

Fig. 6. The mass computed at the peak brightness temperature vs. that computed assuming 20 K for the aperture extracted continuum sources. The faded sources in the top left of the diagram are those with $M(T_{B,max}) > M(20\mathrm{K})$; the circles along the dashed line show their $M(20\mathrm{K})$. The dashed line shows $M(T_{B,max}) = M(20\mathrm{K})$ and the dashed line shows $M(T_{B,max}) = 0.1M(20\mathrm{K})$

interstellar lines, we used the peak brightness temperature of the line as an estimated lower limit on the core temperature.

In the continuum, we measured a 'concentration parameter', which is the ratio of the flux density in a $0.2''$ aperture to that in a $0.2''$-$0.4''$ annulus divided by three to account for the annulus' larger area. A uniform source with $r > 0.4''$ source would have a concentration $C = 1$ by this definition, while an unresolved point source would have a Gaussian profile resulting in $C = 14$. Only one source approaches this extreme, the HII region e5, while the rest have $C \leq 7$. We set the threshold for a 'concentrated' source to be $C > 2$, which is arbitrary, but does a reasonable job of distinguishing the sources with a clear central concentration from those that have none.

Main sequence OB stars and their illuminated ionized nebulae are in principle easily identified by their free-free emission. Starless cores, protostellar cores, and their variants are more difficult to identify, so we used a combination of temperature and concentration parameter to classify them.

We classified each of the 75 hand-selected sources on the following parameters:

1. Free-free dominated sources ($S_{15GHz} > 0.5S_{226GHz}$) are H II regions
2. Free-free contaminated sources ($S_{15GHz} > 0.1S_{226GHz}$) are likely to be dust-dominated but with H II region contamination; these are either dusty sources superposed on or embedded in a large H II region or they are compact, dusty H II regions
3. Starless core candidates were identified as those with cold peak brightness temperatures $T_B < 20$ K and with a high concentration parameter ($C > 2$)
4. Hot core candidates are those with peak $T_B > 50$ K and $C > 2$
5. Extended cold core and hot core candidates are those with $T_B < 20$ and $T_B > 50$ K and $C < 2$
6. The remaining sources with $S_{15GHz} < 0.1S_{226GHz}$ and $50 > T_B > 20$ K were classed as uncertain compact ($C > 2$) or uncertain extended $C < 2$

The classification is a broad guideline for further analysis.

4.5.1. W51e2e mass and temperature estimates from continuum

In a $0.21'' \times 0.19''$ beam (1100×1000 au), the peak flux density toward W51 e2e is 0.38 Jy, which corresponds to a brightness temperature $T_B = 228$ K. This is a lower limit to the surface brightness of the millimeter core, since an optical depth $\tau < 1$ or a filling factor of the emission $ff < 1$ would both imply higher intrinsic temperatures. The implied luminosity, assuming a pure blackbody, is $L = 4\pi r^2 \sigma_{sb} T^4 = 2.4 \times 10^4 L_\odot$. Since any systematic uncertainties imply a higher temperature, this estimate is a lower limit on the source luminosity.

If we assume that $T_{dust} = T_{peak}$ and that the dust is optically thin, we derive a dust mass $M_{dust} \sim 20\ M_\odot$. This mass is not a strict limit in either direction: if the dust is optically thick, there may be substantial hidden or undetected gas, while if the filling factor is low, it may be much hotter and therefore lower in mass. However, simulations and models both predict that the dust will become highly optically thick at radii $r \lesssim 1000$ au (**??**), so it is likely that this measurement provides only a lower limit on the total gas mass surrounding the protostar.

For an independent measurement of the temperature that is not limited to the optically thick regions, we use the CH_3OH lines in band, calculating an LTE temperature that is $200 < T < 600$ K out to $r < 2''$ ($r < 10^4$ au; Section **??**). As noted in Section **??**, these temperatures may be overestimates when the low-J lines of CH_3OH are optically thick, but for now they are the best measurements we have available.

4.6. *Radial mass profiles around the most massive cores*

In Figure 7, we show the radial profiles extracted from the three high-mass protostellar cores in W51: W51 North, W51 e2e, and W51 e8. The plot shows the enclosed mass out to $\sim 1''$ (5400 AU). On larger spatial scales, the enclosed mass rises more shallowly, indicating the end of the core.

All three sources show similar radial profiles, containing up to 3000 $M_\odot$ within a very compact radius of 5400 AU (0.03 pc). However, the temperature structure within these sources is certainly not homogeneous, and very likely a large fraction of the total flux comes from $T \gtrsim 300$ K heated material (Section 4.4; **?**). If the observed dust were all at 600 K, the mass would be $\sim 17\times$ lower, 100 $M_{\odot}$, which we treat as a strict lower bound as it is unlikely that the dust more than $\gtrsim 1000$ au is so warm. Additionally, it is very likely that a substantial mass of cold dust is also present but undetectable because it is hidden by the hotter dust.

4.7. The mass budget on different spatial scales

An evolutionary indicator used for star-forming regions is the amount of mass at a given density; a more evolved (more efficiently star-forming) region will have more mass at high densities. We cannot measure the dense gas fraction directly, but the amount of flux density recovered by an interferometer provides a reasonable approximation.

For the "total" flux density in the region, we use the Bolocam Galactic Plane Survey observations (**??**), which are the closest in frequency single-dish millimeter data available. We assume a spectral index $\alpha = 3.5$ to convert the BGPS flux density measurements at 271.4 GHz to the mean ALMA frequency of 226.6 GHz. The ALMA data (specifically, the 0.2″ 12m-only data) have a total flux 23.2 Jy above a very conservative threshold of 10 mJy/beam in our mosaic; in the same area the BGPS data have a flux of 144 Jy, which scales down to 76.5 Jy. The recovery fraction is 30±3%, where the error bar accounts for a change in $\alpha \pm 0.5$. The threshold of 10 mJy/beam corresponds to a column threshold $N > 1.3\times10^{25}$ cm^{-3} for 20 K dust. This threshold also corresponds to an optical depth of $\tau \approx 0.5$, implying that a large fraction of the cloud is either approaching optically thick or warmer than 20 K. For an unresolved spherical source in the $\sim 0.2''$ beam, this column density corresponds to a volume density $n > 10^{8.1}$ cm^{-3}.

4.8. Chemically Distinct Regions

4.8.1. Observations

The "hot cores" in W51 (e2, e8, and North) are spatially well-resolved and multi-layered. These cores are detected in lines of many different species spanning areas $\sim 5\times10^{3}-10^{4}$ au across.

Surrounding W51e2e, there are relatively sharp-edged uniform-brightness regions in a few spectral lines over the range 51-60 km s^{-1} (Figure 8). Some of these features are elongated in the direction of the outflow, but most have significant extent orthogonal to the outflow, spanning 9500×6600 AU. They are prominent in CH_3OH, OCS, and CH_3OCH_3, weak but present in H_2CO and SO, and absent in HC_3N and HNCO.

Around e8, a similar feature is observed, but in this case CH_3OCH_3 is absent. Toward W51 north, CH_3OH, H_2CO, and SO exhibit the sharp-edged enhancement feature, while the other species do not. The enhancement is from 50-60 km s^{-1}.

By contrast, along the south end of the e8 filament, no such enhanced features are seen; only H_2CO and the lowest transition of CH_3OH are evident.

The relative chemical structures of e2, e8, and IRS2 are relatively similar. The same species are detected in all of the central cores. However, in e2, CH_3OCH_3, CH_3OCHO, CH_3CH_2CN, and Acetone ($[CH_3]_2$ CO) are significantly more extended in e2 than in the other sources. g-CH_3CH_2OH is detected in W51 North, but is weak in e8 and almost absent in e2 (Figures 8, 9, 10, 11).

Different chemical groups exhibit different morphologies around e2. Species that are elongated in the NW/SE direction are associated primarily with the outflow (HC_3N, CH_3CH_2CN). Other species are associated primarily with the extended core (CH_3OCHO, CH_3OCH_3, $[CH_3]_2$ CO). Some are only seen in the compact core (H_2CN, HNCO, NH_2CHO, and vibrationally excited HC_3N). Only CH_3OH and OCS are associated with both the extended core and the outflow, but not the greater extended emission. H_2CCO seems to be associated with only the extended core, but not the compact core. Finally, there are the species that trace the broader ISM in addition to the cores and outflows (H_2CO, ^{13}CS, OCS, $C^{18}O$ and SO). Both HCOOH and N_2D+ are weak and associated only with the innermost e2e core.

4.8.2. Chemical structure: Interpretation

Probably cut P1 here and move the whole thing to "Discussion" The enhancements in noted lines occur as factor of 3-10 increases in the peak brightness of most of the lines shown in Figure 8. These enhancements could occur from increased total column density, increased abundance of the molecules, or increased excitation.

In Section 4.9, we examine the CH_3OH abundance and excitation conditions. The detection of highly excited CH_3OH lines, including $18_{3,15} - 17_{4,14}$ ($E_U = 447$ K) and $25_{3,22} - 24_{4,20}$ ($E_U = 802$ K), suggests that excitation is part of the explanation for the brighter molecular emission. However, LTE modeling reveals that the CH_3OH abundance increases by a factor of $\sim 5-10$ from the protocluster gas inward toward the e2e core. This abundance gradient is likely present in other molecules as well. Given the enhanced abundance of CH_3OH, these sharp-edged bubbles probably represent sublimation zones in which substantial quantities of grain-processed materials are released into the gas phase. The relatively sharp edges likely reflect the particular point where the temperature exceeds the sublimation temperature for each species.

4.9. CH_3OH temperatures & columns in the hot cores

The extreme chemical regions appear to be associated with regions of elevated gas temperature. We examine this directly by analyzing the excitation of lines for which we have detected multiple transitions with significant energy differences. We do not use H_2CO for this analysis because it is clearly optically thick (self-absorbed) in all lines in the regions of greatest interest.

We produce rotational diagrams for each spatial pixel covering all CH_3OH lines detected at high significance toward at least one position. The detected lines span a range $45 < E_U < 800$ K, allowing robust measurements of the temperature assuming the lines are optically thin, in LTE, and the gas temperature is high enough to excite the lines. These conditions are likely to be satisfied in the e2e, e8, and North cores, except for the optically thin requirement. Luckily, there are some lines in band that have much lower Einstein $A_{i,j}$ values but comparable upper-state energy lev-

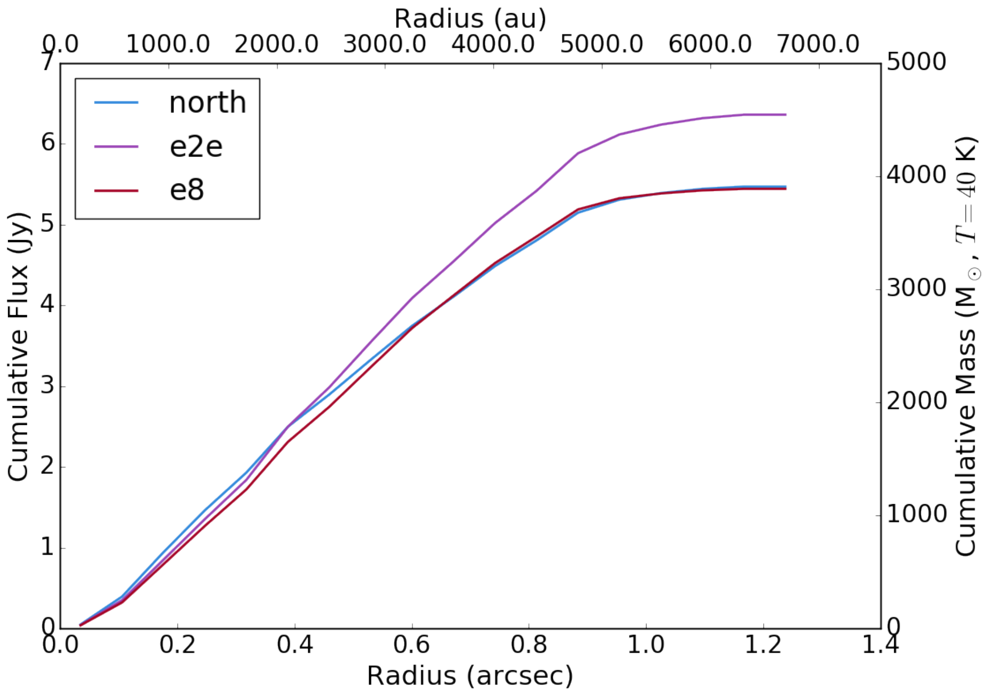

Fig. 7. The cumulative flux density radial profiles centered on three massive protostellar cores. They share similar profiles and are likely dominated by hot dust in their innermost regions, but they are more likely to be dominated by cooler dust in their outer, more massive regions. The cumulative mass distribution may therefore be deceptive.

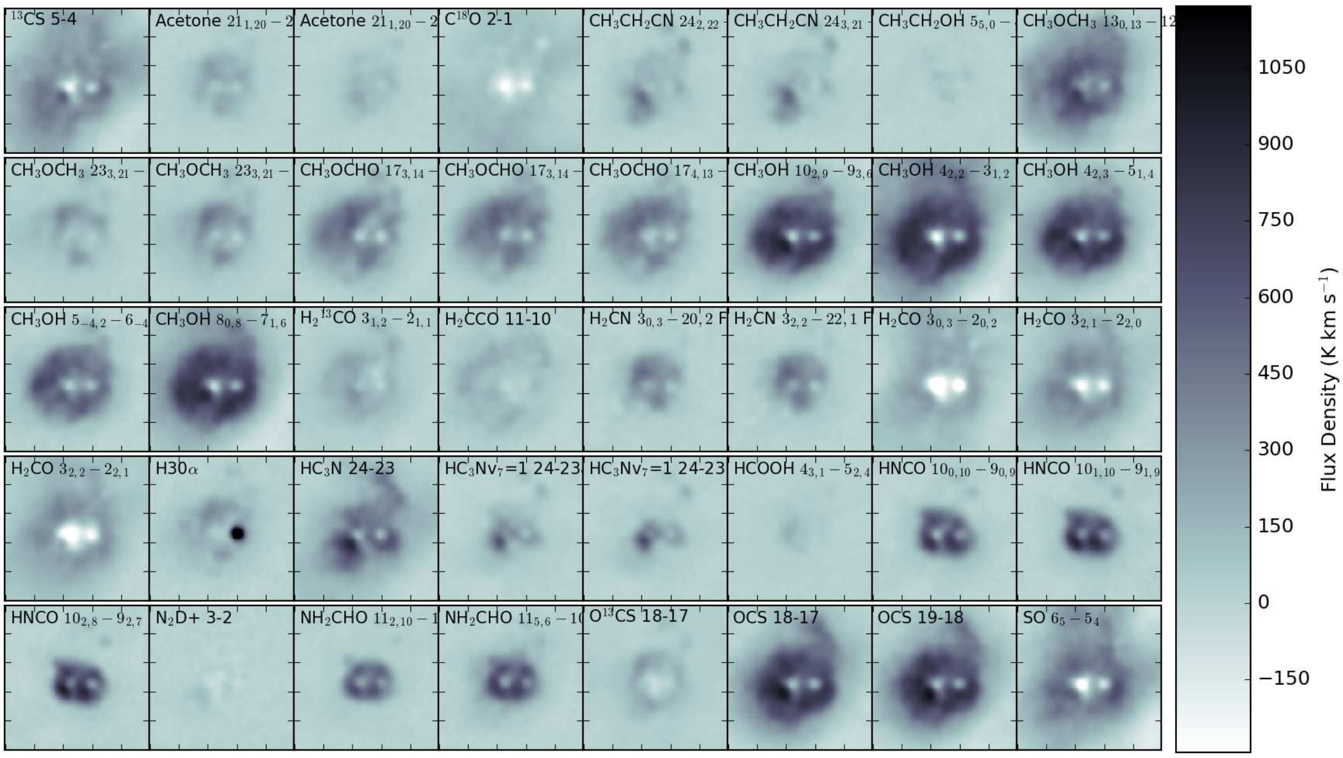

Fig. 8. Moment 0 maps of the e2 region in 40 different lines over the range 51 to 60 km s^{-1} with continuum subtraction using the 30th percentile emission over the ranges 25-40 and 75-90 km s^{-1}. All images are on the same scale, and the negative features show absorption against the continuum. There is a strong 'halo' of emission seen in the CH_3Ox lines and OCS. Extended emission is also clearly seen in SO, ^{13}CS, and H_2CO, though these lines more smoothly blend into their surroundings. HNCO and NH_2CHO have smaller but substantial regions of enhancement with a sharp contrast to their surroundings. HC_3N traces the e2 outflow. The bright H30α emission marks the position of e2w, the hypercompact HII region that dominates the centimeter emission in e2.

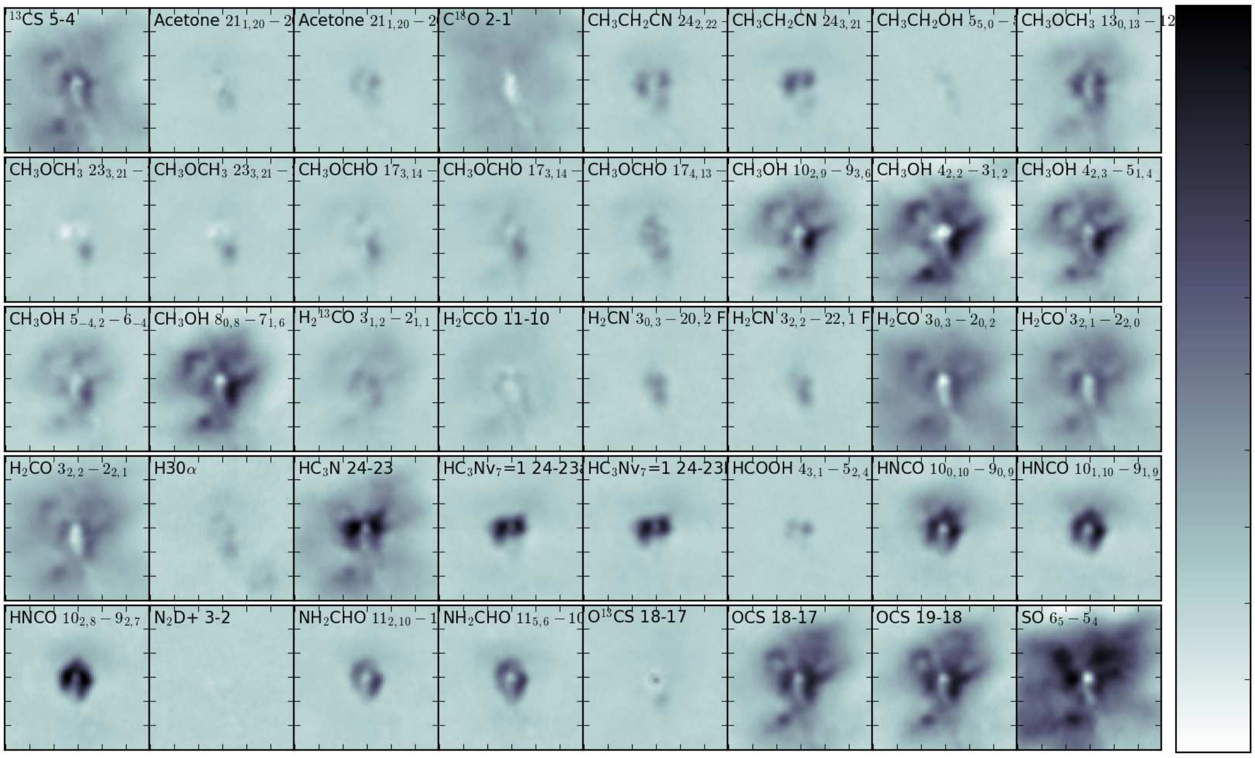

Fig. 9. Moment 0 maps of the e8 region in 40 different lines over the range 52 to 63 km s^{-1} with continuum subtraction using the 30th percentile emission over the ranges 25-40 and 75-90 km s^{-1}. All images are on the same scale, and the negative features show absorption against the continuum. As in e2, there is extended emission in the CH$_3$OH and OCS lines, but in contrast, the othe CH$_3$Ox lines are more compact. SO is brighter than OCS in e8, whereas the opposite is true in e2.

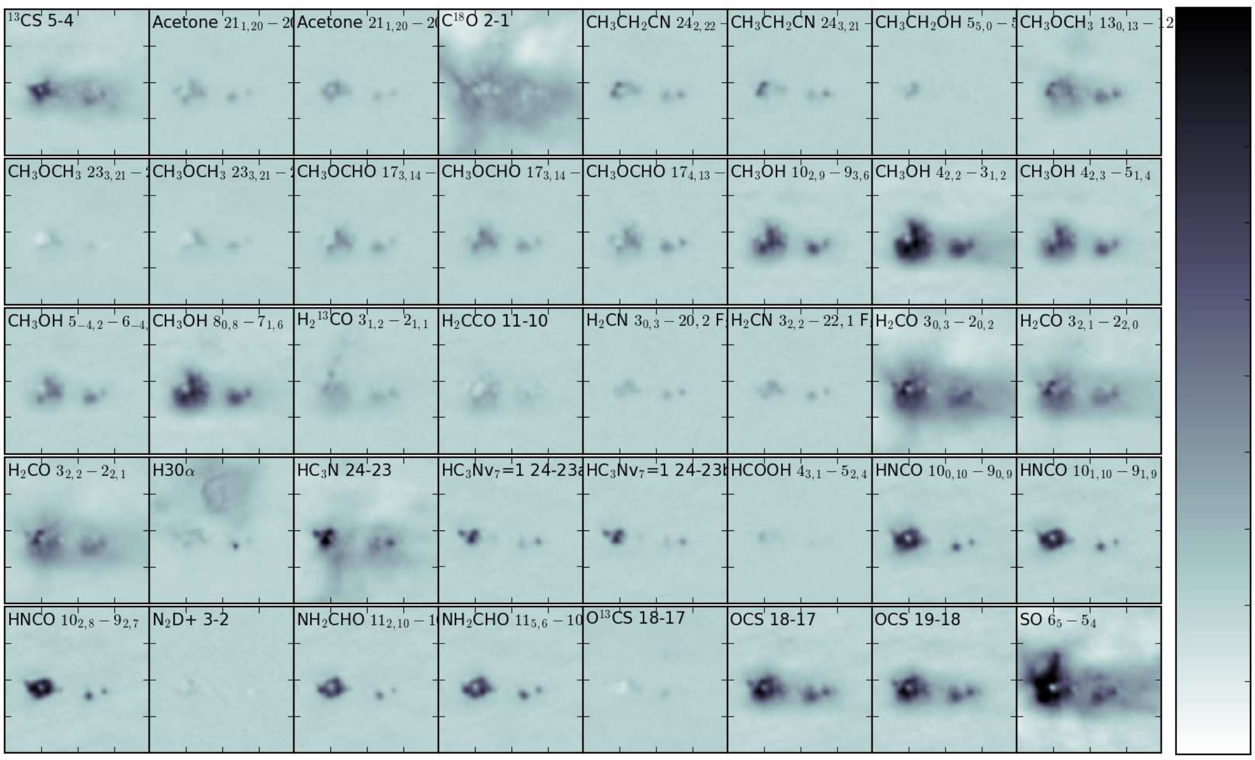

Fig. 10. Moment 0 maps of the W51 IRS2 region in 40 different lines over the range 54 to 64 km s^{-1} with continuum subtraction using the 30th percentile emission over the ranges 25-40 and 75-90 km s^{-1}. All images are on the same scale, and the negative features show absorption against the continuum. Qualitatively, the relative extents of species seem comparable to e8. The H30α point source is W51 d2.

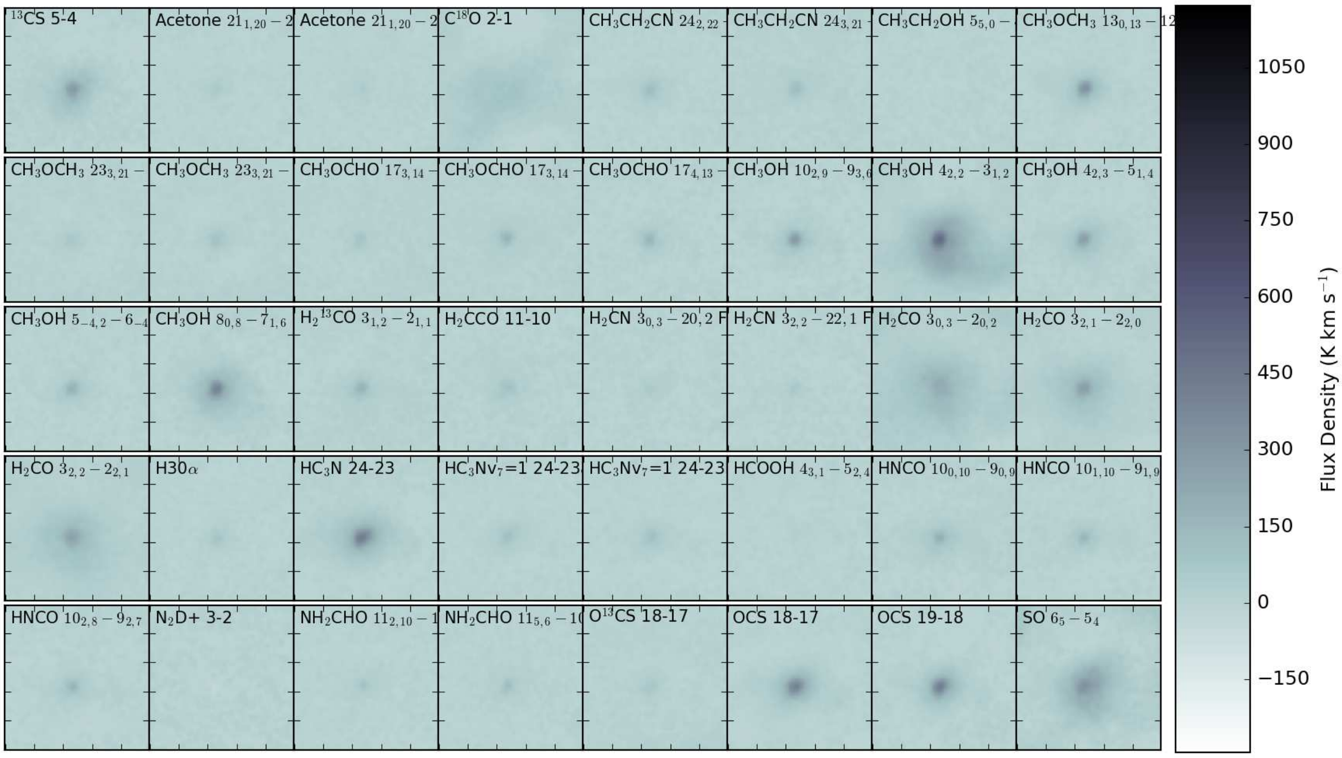

Fig. 11. Moment 0 maps of the ALMAmm14 region in 40 different lines over the range 58 to 67 km s^{-1} with continuum subtraction using the 30th percentile emission over the ranges 25-40 and 75-90 km s^{-1}. All images are on the same scale. ALMAmm14 is one of the brightest sources outside of e2/e8/IRS2, but it is substantially fainter than those regions. Still, it has a noticeably rich chemistry.

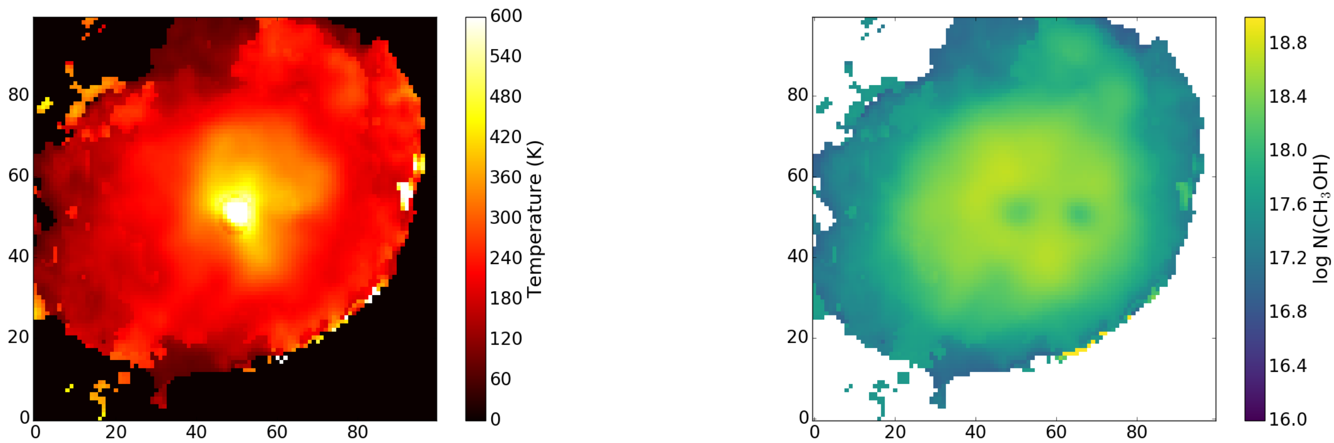

(a)

(b)

Fig. 12. Methanol temperature and column density maps around e2. The central regions around the cores appear to have lower column densities because the lines become optically thick and self-absorbed.

els, allowing us to probe higher column densities than would otherwise be possible.

Sample fitted rotational diagrams are displayed in Figure 13. The line intensities are computed from moment maps integrating over the range (51, 60) km s^{-1} in continuum-subtracted spectral cubes, where the continuum was estimated as the median over the ranges (25-35,85-95) km s^{-1}, except for the J=25 lines, which had a continuum estimated from the 10th percentile over the same range to exclude contamination from the SO outflow line wings.

To validate some of the rotational diagram fits, we examined the modeled spectra overlaid on the real (Figure 14). These generally display significant discrepancies, especially at low J where self-absorption is evident. In Figure 14, there is clearly a low-temperature component slightly redshifted from the high-J peak that can be seen as a dip within the line profile. The presence of this unmodeled low-

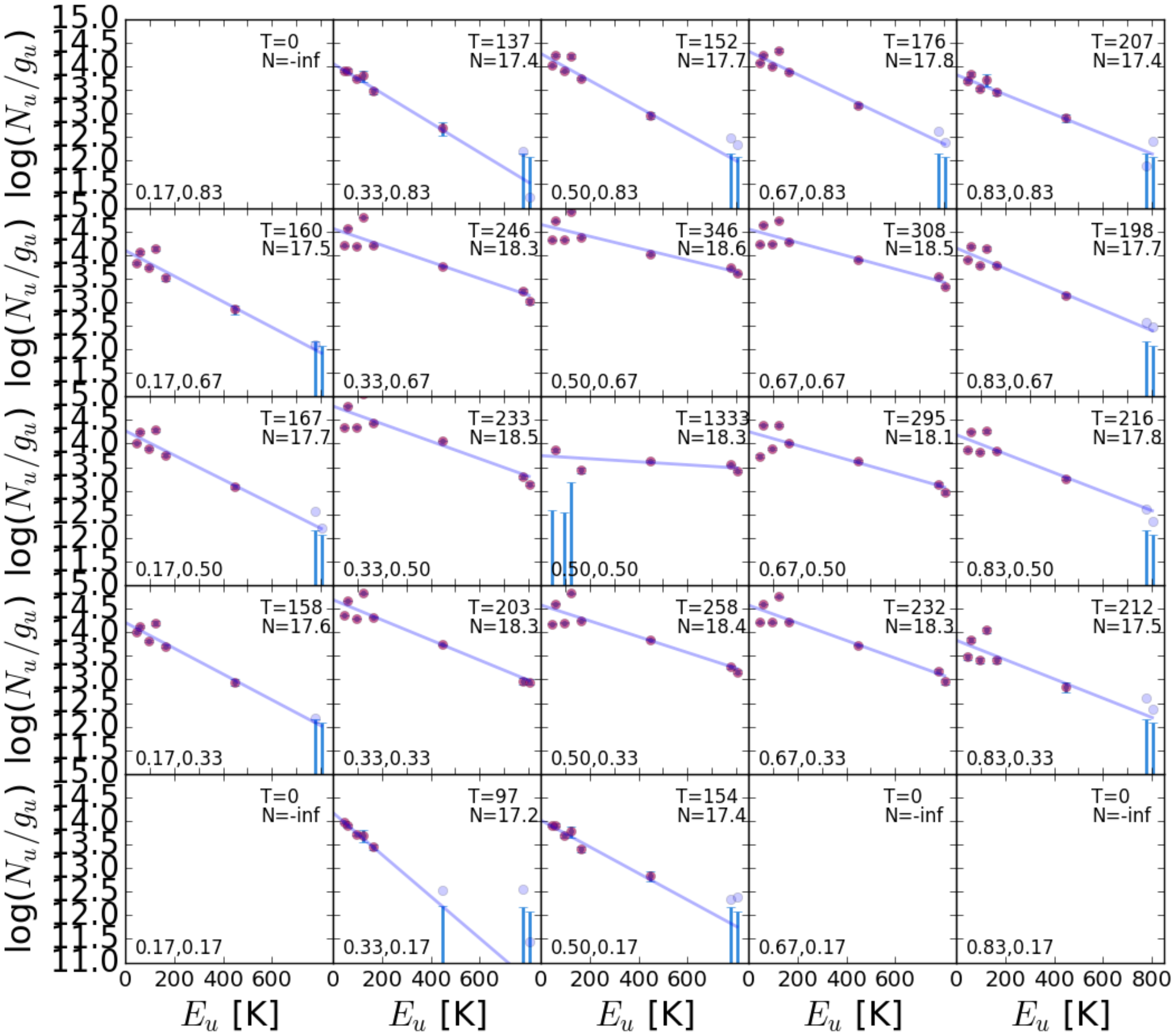

Fig. 13. A sampling of fitted rotation diagrams of the detected CH_3OH transitions. These are meant to provide validation of the temperatures and column densities derived and shown in Figure 12. The lower-left corner shows the position from which the data were extracted in that figure in units of figure fraction. The horizontal black lines show the detection threshold of each of the transitions; points below these lines are ignored when fitting, and instead the threshold itself is used. The fitted temperature and column are shown in the top right of each plot.

temperature component renders our CH_3OH temperature measurements uncertain.

Figure 15 shows a comparison between the CH_3OH $10_{2,9} - 9_{3,6}$ line and the 225 GHz continuum. While the brightest regions in CH_3OH mostly have corresponding dust emission, the dust morphology traces the CH_3OH morphology very poorly. This difference suggests that the enhanced brightness is not simply because of higher total column density. We examine the dust-CH_3OH link more quantitatively in Figure 17.

Figure 16 shows the observed brightness profiles of CH_3OH line and dust continuum emission. Figure 17 shows a comparison of the CH_3OH temperature and abundance. The CH_3OH abundance is derived by comparing the rotational diagram (RTD) fitted CH_3OH column density to the dust column density while using the CH_3OH-derived temperature as the assumed dust temperature. The figure shows all pixels within a $3''$ (16200 AU) radius of e2e, with pixels having low column density and high temperature (i.e., pixels with bad fits) and those near e2w (which may be heated by a different source) excluded. We used moment-0 (integrated intensity) maps of the CH_3OH lines to perform these RTD fits, which means we have ignored the line profile entirely and in some cases underestimated the intensity of the optically thick lower-J lines: in the regions of highest column, the column is underestimated and the temperature is overestimated, as can be seen in Figure 14.

A few features illustrate the effects of thermal radiative feedback on the gas. The temperature jump starting inwards of $r \sim 1.5''$ (8100 AU; Figure 17b) is substantial, though the 100-200 K floor at greater radii is likely artificial

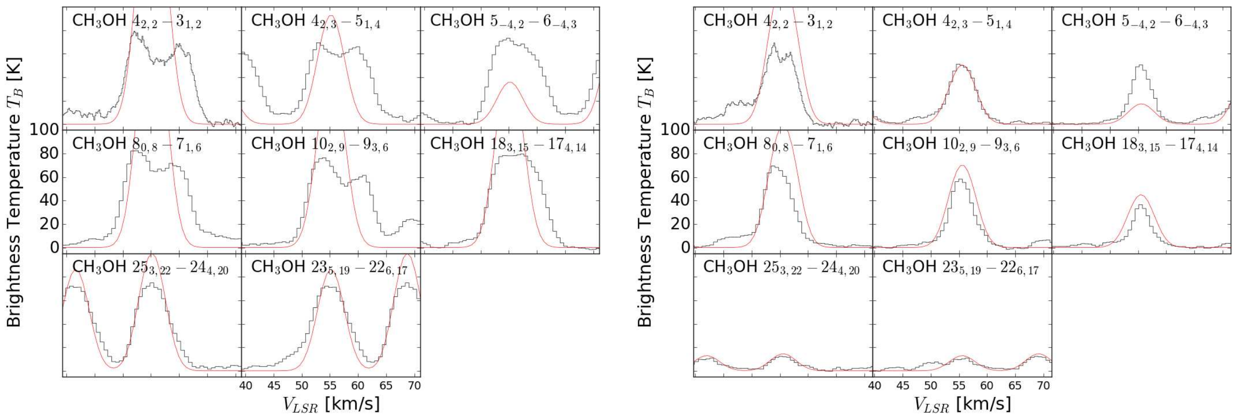

(a) (b)

Fig. 14. Spectra of the CH_3OH lines toward a selected pixel just outside of the e2e core. The red curves show the LTE model fitted from a rotational diagram as shown in Figure 13. The model is not a fit to the data shown, but is instead a single-component LTE model fit to the integrated intensity of the lines shown. As such, the fit is not convincing, and it is evident that a single-temperature, single-velocity model does not explain the observed lines. Nonetheless, a component with the modeled temperature is likely to be present in addition to a cooler component responsible for the self-absorption in the low-J lines. (a) shows a pixel close to the center of e2e, which is probably optically thick in most of the shown transitions, while (b) shows a better case where the highest-A_{ij} lines are overpredicted but many of the others are well-fit.

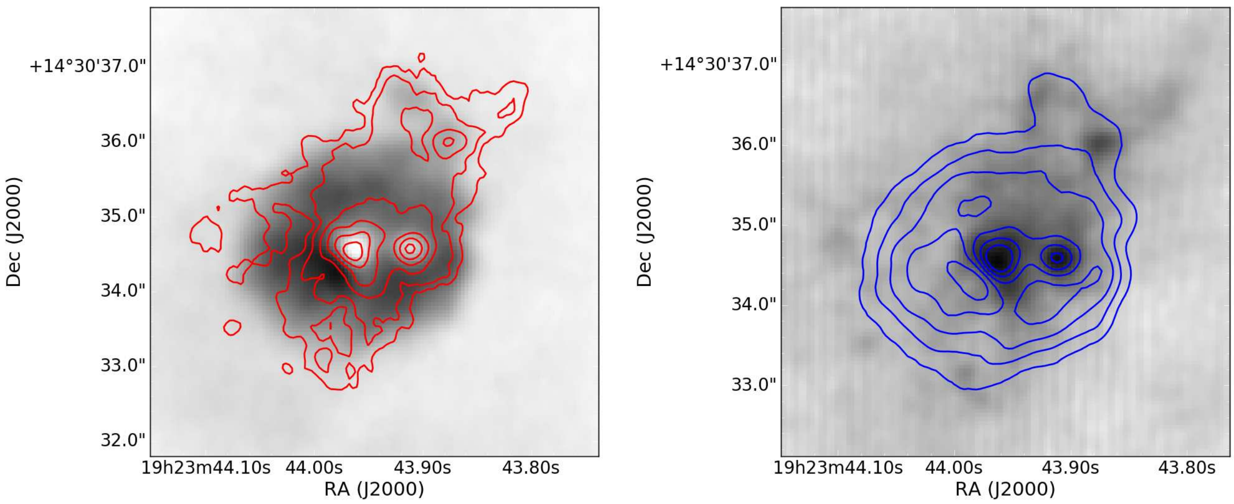

(a) (b)

Fig. 15. Images showing CH_3OH $10_{2,9} - 9_{3,6}$ and 225 GHz continuum emission, with CH_3OH in grayscale and continuum in contours (left) and continuum in grayscale, CH_3OH in contours (right). The fainter (whiter) regions in the center of the CH_3OH map correspond to the bright continuum cores and show where all lines appear to be self-absorbed.

as the low-J transitions are not consistent with a thermal distribution. There is an abundance enhancement at the inner radii, but it appears to be a radial bump rather than a pure increase. The abundance enhancement is probably real, and is approximately a factor of $\sim 5 - 10$. The inner abundance dip is caused by two coincident effects: first, the CH_3OH column becomes underestimated because the CH_3OH is *self*-absorbed, and second, the dust becomes optically thick, blocking additional CH_3OH emission, though this latter effect is somewhat self-regulating since it also decreases the dust column (the denominator in the abundance expression).

4.10. Ionizing vs non-ionizing radiation

The formed and forming protostars are producing a total $\gtrsim 10^7$ $L_\odot$ of far infrared illumination (?). This radiation heats the cloud's molecular gas, affecting the initial conditions of future star formation.

The ionizing radiation in W51 was discussed in detail in (?). Ionizing radiation affects much of the cloud, but little of the high-density prestellar material. There is no evidence of increased gas temperatures in the vicinity of H II regions. While in Section 4.10 we identify chemically enhanced regions as those where radiative feedback has heated the dust and released ices into the gas phase, no such regions are observed surrounding the most luminous compact H II regions.

This lack of molecular brightness enhancement is only an indirect indication that the H II regions do not affect

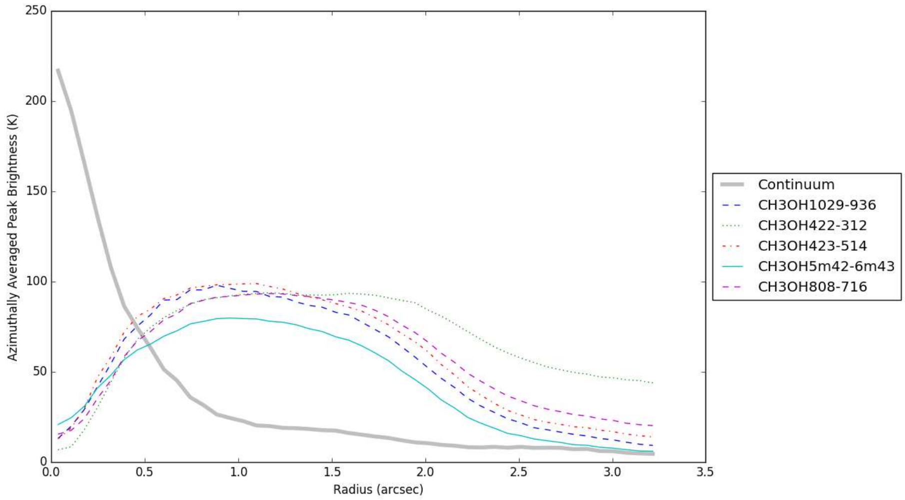

Fig. 16. Radial profiles of the peak surface brightness of five CH_3OH transitions along with the profile of the continuum brightness. The radial profiles were constructed from images with $0.2''$ resolution including only 12m data. The central dip shows where the lines go into absorption, though they are only seen in absorption at ~ 55 km s^{-1}. The CH_3OH lines are continuum-subtracted.

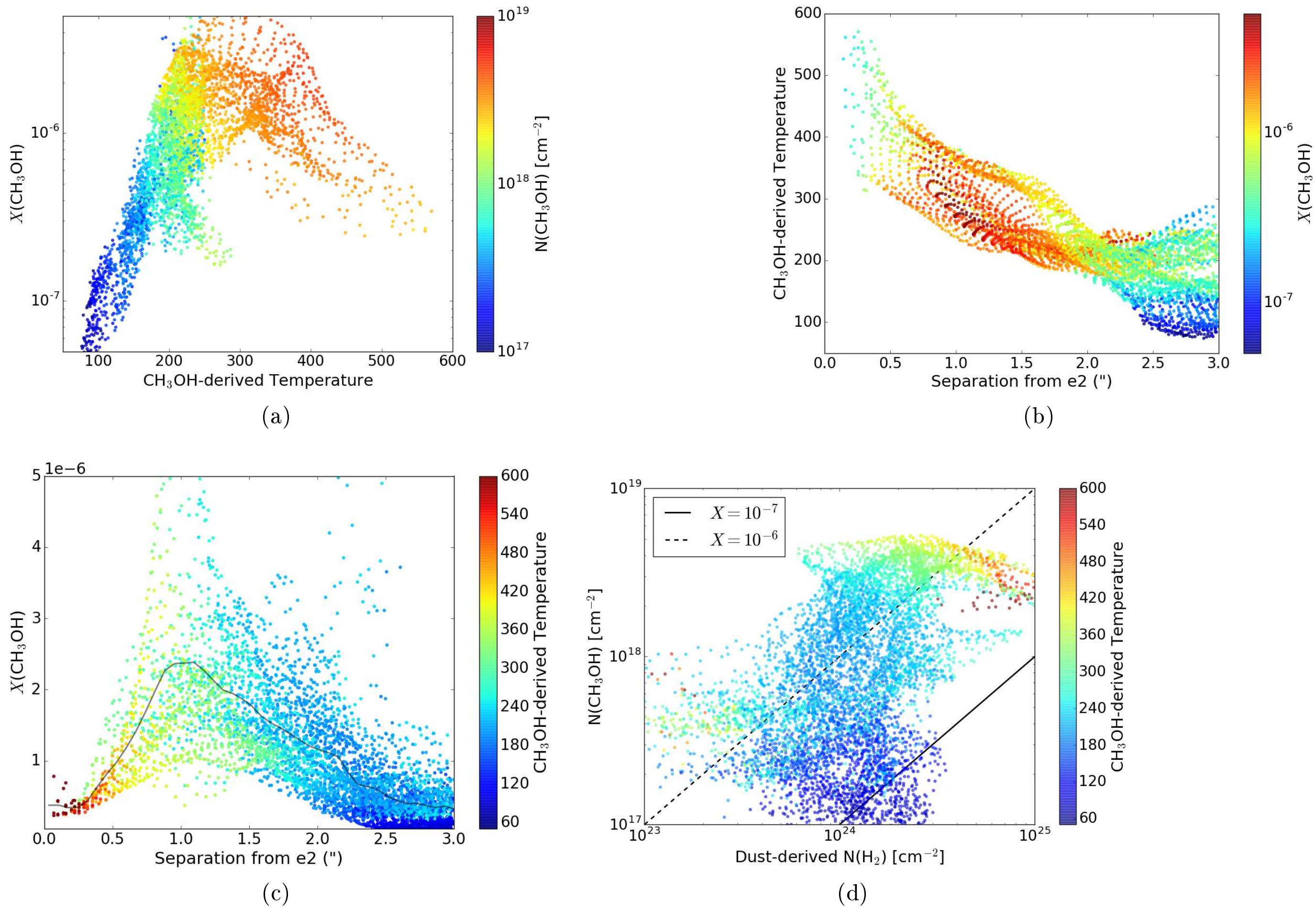

Fig. 17. Comparison of the CH_3OH temperature, column density, and abundance. (a) The relation between temperature and abundance. There is a weak correlation, but most of the high abundance regions are at high temperatures. (b) Temperature vs distance from e2e. There is a clear trend toward higher temperatures closer to the central source (c) Abundance vs distance from e2e. The apparent dip at $r < 1''$ is somewhat artificial, as it is driven by a rising dust emissivity that corresponds to an increasing optical depth in the dust. The CH_3OH column in this inner region is likely to be underestimated. (d) CH_3OH vs dust column density.

the surrounding dense gas temperature. A direct proof that the ionizing sources are having no or minimal effect would require temperature measurements on the outskirts of the H II regions, but this is not possible without prior detection of bright emission in thermometric transitions.

The chemical maps shown in Section 4.8 show the volumes of gas clearly affected by newly-forming high-luminosity stars. The CH_3OH-enhanced region around W51e2 extends 0.04 pc, or 8500 AU (see Section 4.9). Other locally enhanced species, especially the nitrogenic molecules HNCO and NH_2CHO, occupy a smaller and more asymmetric region around e2e and e2w (Figure 18). These chemically enhanced regions are most prominent around the weakest radio sources or regions with no radio detection; they are most likely heated by direct infrared radiation from these sources.

4.11. Outflows

We detected many outflows, primarily in CO 2-1 and SO $6_5 - 5_4$. The flows are weakly detected in some other lines, e.g. H_2CO, but we defer discussion of outflow chemistry to a future work.

In this section, we discuss some of the unique outflows and unique features of outflows in the W51 region. We show the most readily identified outflows in Figures 22, 21, 23, and 24.

4.11.1. The Lacy jet

A high-velocity outflow was discovered within the W51 IRS2 region by **?**, and subsequently detected in H77α by **?**. We have discovered the CO counterpart to this outflow, which comes from near the continuum source ALMAmm31 (Figure 20). Strangely, though, the outflow is not directly centered on the continuum source, but is slightly offset. The outflow shows red- and blue-shifted flows that form the base of the ionized outflow reported by **?**, Figure 21.

4.11.2. north

The outflow from W51 north is extended and complex. A jet-like high-velocity feature appears directly to the north of W51 north in both CO and SO (Figure 21). However, in SO, this feature begins to emit at ~ 47 km s^{-1} and continues to ~ 100 km s^{-1}. The CO emission below < 70 km s^{-1} is completely absent, presumably obscured by foreground material. The blueshifted component, by contrast with the red, points to the southeast and is barely detected in CO, but again cleanly in SO. It is sharply truncated, extending only $\sim 1''$ (~ 5000 AU). Unlike the Lacy jet, there is no evidence that this outflow transitions into an externally ionized state.

The northernmost point of the W51 North outflow may coincide with the **?** H_2 and [Fe II] outflow. There is some CO 2-1 emission coincident with the southernmost point of the H_2 features, and these all lay approximately along the W51 North outflow vector. However, the association is only circumstantial.

4.11.3. The e2e outflow

The dominant outflow in W51, which was previously detected by the SMA (**??**), comes from the source e2e. This outflow is remarkable for its high velocity, extending nearly to the limit of our spectral coverage. The ends of the flow cover at least $-50 < v_{lsr} < 160$ km s^{-1}, or a velocity $v \pm 100$ km s^{-1}.

The morphology is also notable. Both ends of the outflow are sharply truncated at $\sim 2.5''$ (0.07 pc) from e2e (Figure 22). To the southeast, the high-velocity flow lies along a line that is consistent with the extrapolation from the northwest flow, but at lower velocities ($10 < v_{LSR} < 45$ km s^{-1}), it jogs toward a more north-south direction (Figure 23). In the northwest, the redshifted part of this flow ($70 < v_{LSR} < 120$ km s^{-1}) apparently collides with a *blue*shifted flow from another source ($22 < v_{LSR} < 45$ km s^{-1}), suggesting that these outflows intersect, though such a scenario seems implausible given their small volume filling factor.

The extreme velocity and morphology carry a few implications for the accretion process in W51. The sharp symmetric truncation, combined with the extraordinary velocity, suggests that the outflow is freshly carving a cavity in the surrounding dense gas. The observed velocities are high enough that their bow shocks likely dissociated all molecules, so some ionized gas is likely present at the endpoints; this ionized gas has not been detected in radio images because of the nearby 100 mJy HCHII region e2w. The dynamical age of the outflow is ~ 600 years at the peak observed velocity, which is a lower limit on the true age of the outflow.

4.11.4. e8

There are at least four distinct outflows coming from the e8 filament. The e8 core is launching a redshifted outflow to the northwest. A blueshifted outflow is coming from somewhere south of the e8 peak and pointing straight east. While these originate quite near each other, they seem not to have a common source, since the red and blue streams are not parallel (Figures 22 and 24). The e8 outflows are too confused and asymmetric for simple interpretation.

5. Discussion

5.1. The scales and types of feedback

The most promiment features of our observations are the warm, chemically enhanced regions surrounding the highest dust concentrations, and the corresponding *lack* of such features around the ionized nebulae. This difference implies that the immediate star formation process - that of gas collapse and fragmentation from a molecular cloud - is primarily affected by feedback from other forming stars, *not* from previous generations of now-exposed stellar photospheres.

On the scales relevant to the fragmentation process, i.e., the ~ 0.1 pc scales of prestellar cores, this decoupling can be explained simply. Stellar light is produced mostly in the UV, optical, and near-infrared. As soon as a star is exposed, either by consuming or destroying its natal core, that light is able to stream to relatively large ($\gtrsim 1$ pc) scales before being absorbed. At that point, the stellar radiation is poorly coupled to the scales of direct star formation. By contrast, stars embedded in their natal cores will have all of their light reprocessed from UV/optical/NIR to the far-IR within a < 0.1 pc sphere, providing a far-infrared background light capable of heating its surroundings.

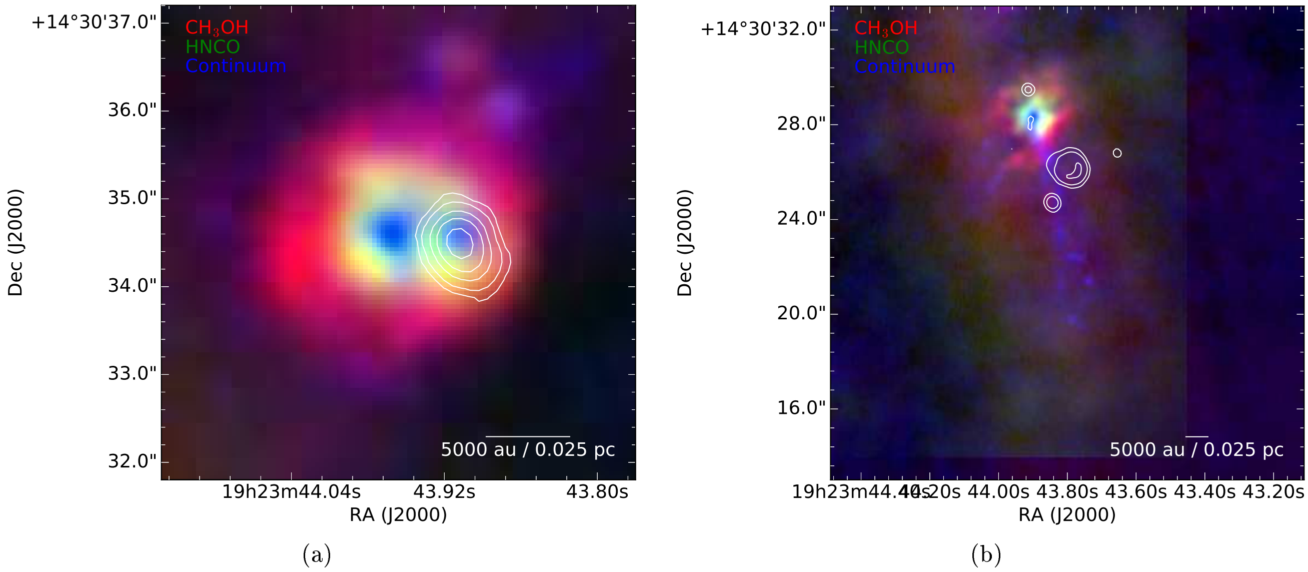

Fig. 18. Image of CH_3OH $8_{0,8} - 7_{1,6}$ (red), HCNO $10_{0,10} - 9_{0,9}$ (green), and 225 GHz continuum (blue) toward (a) W51e2 (b) W51e8. The contours show Ku-band radio continuum emission tracing the H II regions (a) W51 e2w and (b) W51e1, e3, e4, e9, and e10. The CH_3OH emission is relatively symmetric around the high-mass protostar W51 e2e and the weak radio source W51 e8, suggesting that these forming stars are responsible for heating their surroundings. By contrast, the H II regions do not exhibit any local molecular brightness enhancements (except e8), indicating that the H II regions are not heating their local dense molecular gas.

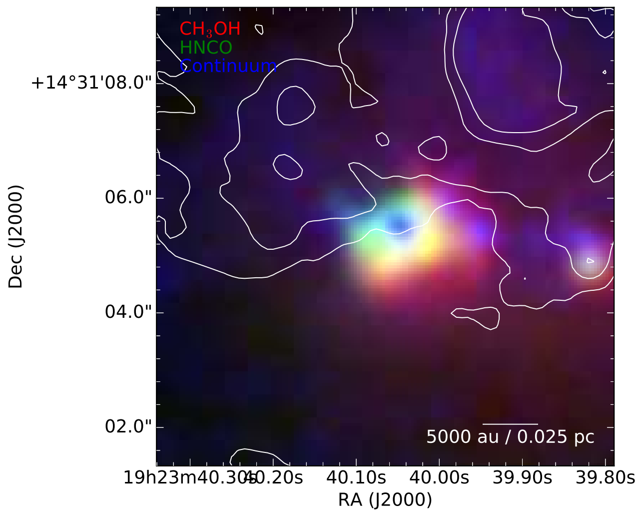

Fig. 19. Image of CH_3OH $8_{0,8} - 7_{1,6}$ (red), HCNO $10_{0,10} - 9_{0,9}$ (green), and 225 GHz continuum (blue) toward north, as in Figure 18. The contours show Ku-band radio continuum emission tracing the diffuse IRS 2 H II region.

The different effects of ionizing vs thermal radiation can be seen directly in the three main massive star forming regions, e2, e8, and north. Figures 18 and 19 show both the highly-excited warm molecular gas in color and the free-free emission from ionized gas in contours. As described in Section 4.10, the spatial differences indicate that the ionizing radiation sources - the exposed OB stars - have little effect on the star-forming collapsing and fragmenting gas.

The low impact of photospheric radiation on collapsing gas suggests that second-generation star formation is relatively unaffected by its surroundings. Instead, the stars of the same generation - those currently embedded and accreting - have the dominant regulating effect on the gas. The formation of the stellar initial mass function *within clusters* is therefore predominantly self-regulated, with little external influence.

5.1.1. Outflows

While the outflows described in Section 4.11 are impressive and plentiful, they are obviously not the dominant form of feedback, as their area filling factor is small compared to that of the various forms of radiative feedback. A low area filling factor implies a substantially smaller volume filling factor and therefore a lower overall effect on the cloud. However, these outflows likely do punch holes through protostellar envelopes and the surrounding cloud material, allowing radiation to escape.

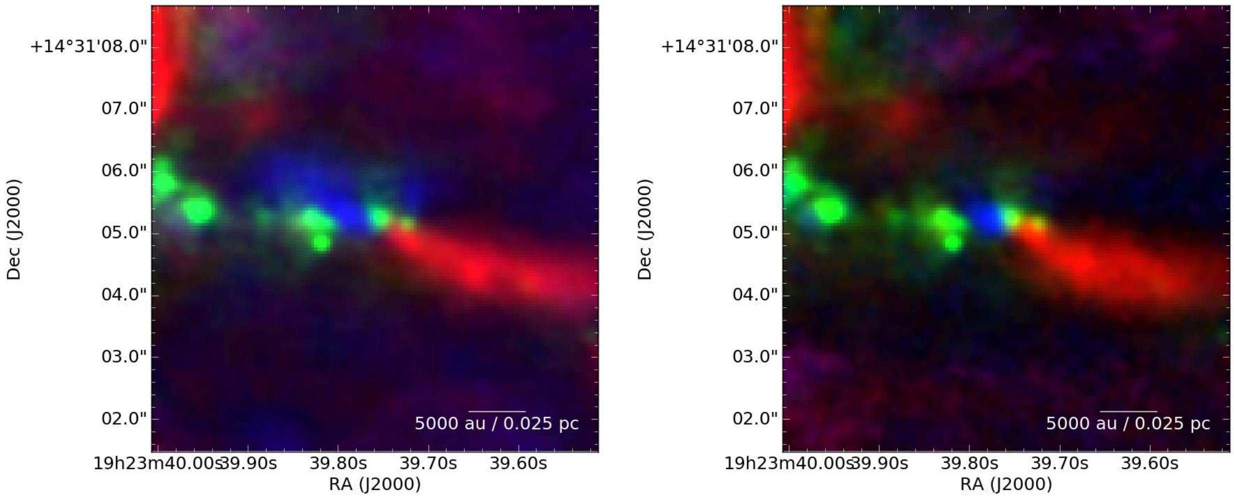

(a) (b)

Fig. 20. Outflows shown in red and blue for (a) CO 2-1 and (b) SO $6_5 - 5_4$ with continuum in green. This symmetric molecular outflow forms the base of the **?** ionized outflow detected further to the east. The continuum source is offset from the line joining the red and blue outflow lobes.

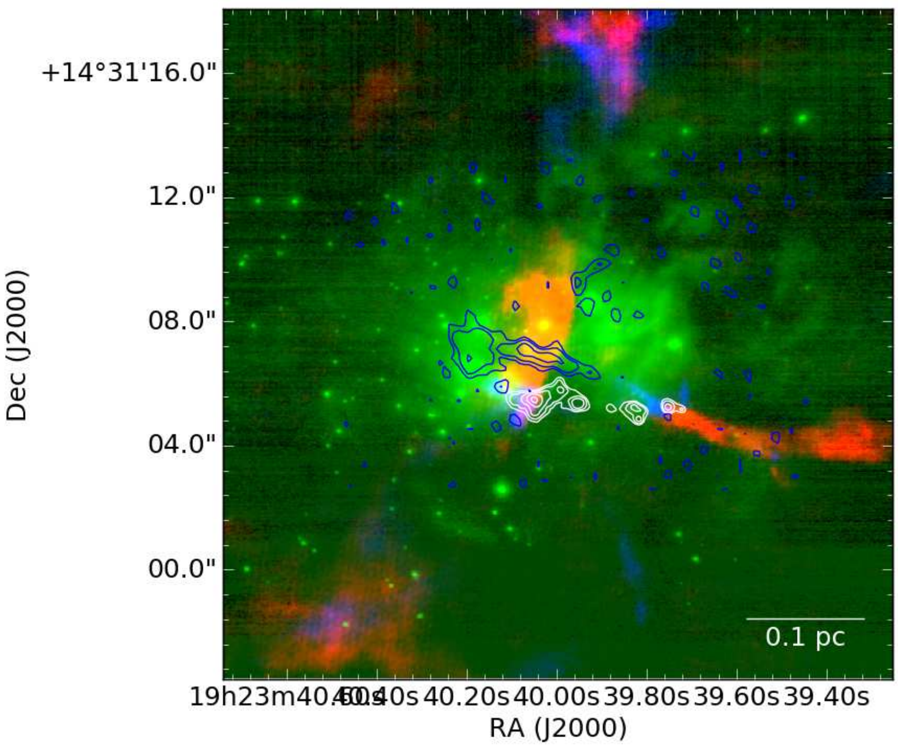

Fig. 21. Outflows in the W51 IRS2 region. The green emission is NACO K-band continuum (**?**), with ALMA 1.4 mm continuum contours in white and H77α contours in blue. The **?** jet is prominent in H77α.

The detection of widespread high-J CH_3OH emission around the highest-mass protostars suggests that the use of CH_3OH as a bulk outflow tracer as suggested by **?** is not viable in regions with forming high-mass stars. While mid-J CH_3OH emission is detected associated with the outflow (e.g., the J=10-9 transition), it is completely dominated by the general 'extended hot core' emission described in Section 4.8.

5.2. The accreting phase of high-mass star formation

The strong outflows observed around the highest-mass forming stars, e2e, e8, and north are clear indications of ongoing accretion onto these sources. However, the bright H II regions, including e2w, e1, and d2, all lack any sign of an outflow or a surrounding rotating molecular structure. Most of these sources lack any surrounding molecular material at all.

Some models of high-mass star formation suggest that accretion continues through the ionized (H II region) phase

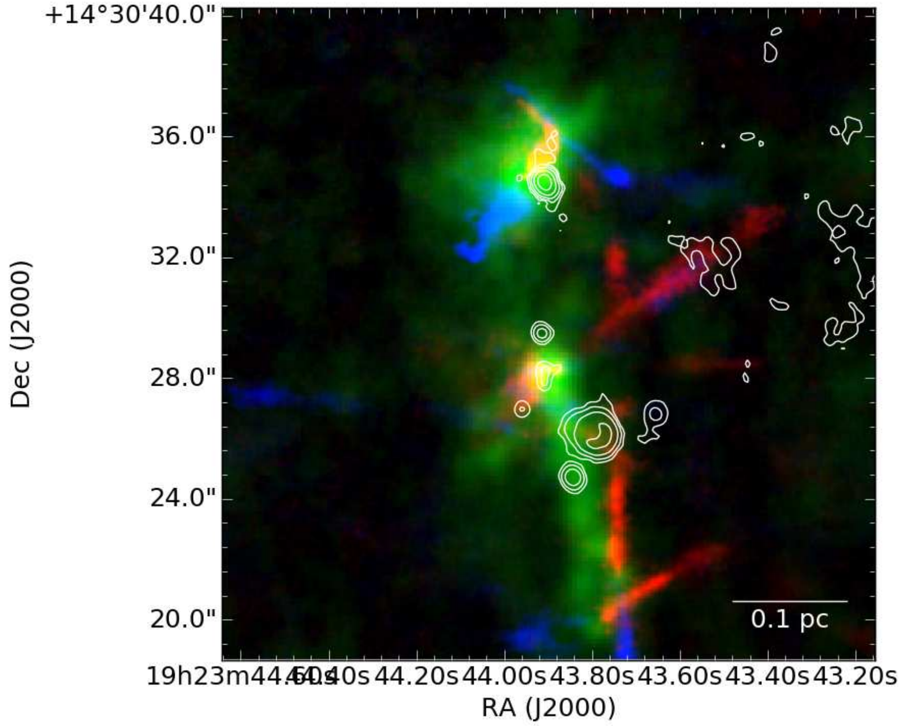

Fig. 22. Outflows in red and blue overlaid on mm continuum in green with cm continuum contours in white. The northern source is e2, the southern source at the tip of the long continuum filament is e8.

(**?**). The lack of molecular material around the majority of the compact H II regions in W51 suggests instead that most of the accretion is done by the time an H II region ignites.

5.3. Jeans analysis?

Fragmentation is one of the critical problems in high-mass star formation. Assuming typical initial conditions for molecular clouds, with temperatures of order 10 K, gas is expected to fragment into sub-solar mass cores, preventing material from accreting onto single high-mass stars (**?**). Even after high-mass stars successfully form, further fragmentation could halt the growth of these stars and limit their final mass (**?**).

Thermal Jeans fragmentation can be limited or suppressed entirely if the gas is warm enough. The high observed gas temperatures, $T \sim 100 - 600$ K over $\sim 10^4$ AU, around the high mass protostars indicate that their radiative feedback in the infrared has a dramatic effect on the gas.

Is it worth going through the process of preventing/halting fragmentation by heating? Should probably compute density profile, temperature profile, resulting jeans mass profile

6. Conclusions

We conclude.

Appendix A: A bubble around e5

There is evidence of a bubble in the continuum around e5 with a radius of 6.2″ (0.16 pc; Figure A.1). The bubble is completely absent in the centimeter continuum, so the observed emission is from dust. The bubble edge can be seen from 58 km s^{-1} to 63 km s^{-1} in C^{18}O and H$_2$CO, though it is not continuous in any single velocity channel. There is a collection of compact sources (protostars or cores) along the southeast edge of the bubble.

The presence of such a bubble in dense gas, but its absence in ionizing gas, is surprising. The most likely mechanism for blowing such a bubble is ionizing radiative feedback, especially around a source that is currently a hypercompact HII region, but since no free-free emission is evident within or on the edge of the bubble, it is at least not presently driving the bubble. A plausible explanation for this discrepancy is that e5 was an exposed O-star within the past Myr, but has since begun accreting heavily and therefore had its HII region shrunk. This model is marginally supported by the presence of a 'pillar' of dense material pointing from e5 toward the south.

The total flux in the north half of the 'bubble', which shows no signs of free-free contamination, is about 1.5 Jy. The implied mass in just this fragment of the bubble is about $M \sim 350\ M_\odot$ for a relatively high assumed temperature $T = 50$ K. The total mass of the bubble is closer to $M \sim 1000\ M_\odot$, though it may be lower ($\sim 500\ M_\odot$) if the southern half is dominated by free-free emission.

With such a large mass, the implied density of the original cloud, assuming it was uniformly distributed over a 0.2 pc sphere, is $n(\mathrm{H}_2) \approx 2 - 5 \times 10^5$ cm^{-3}.

To evaluate the plausibility of the H II-region origin of the bubble, we compare to classical equations for H II regions. The Strömgren radius is

$$R_\mathrm{s} = \left(\frac{3Q_\mathrm{H}}{4\pi\alpha_\mathrm{B} n^2}\right)^{\frac{1}{3}}. \tag{A.1}$$

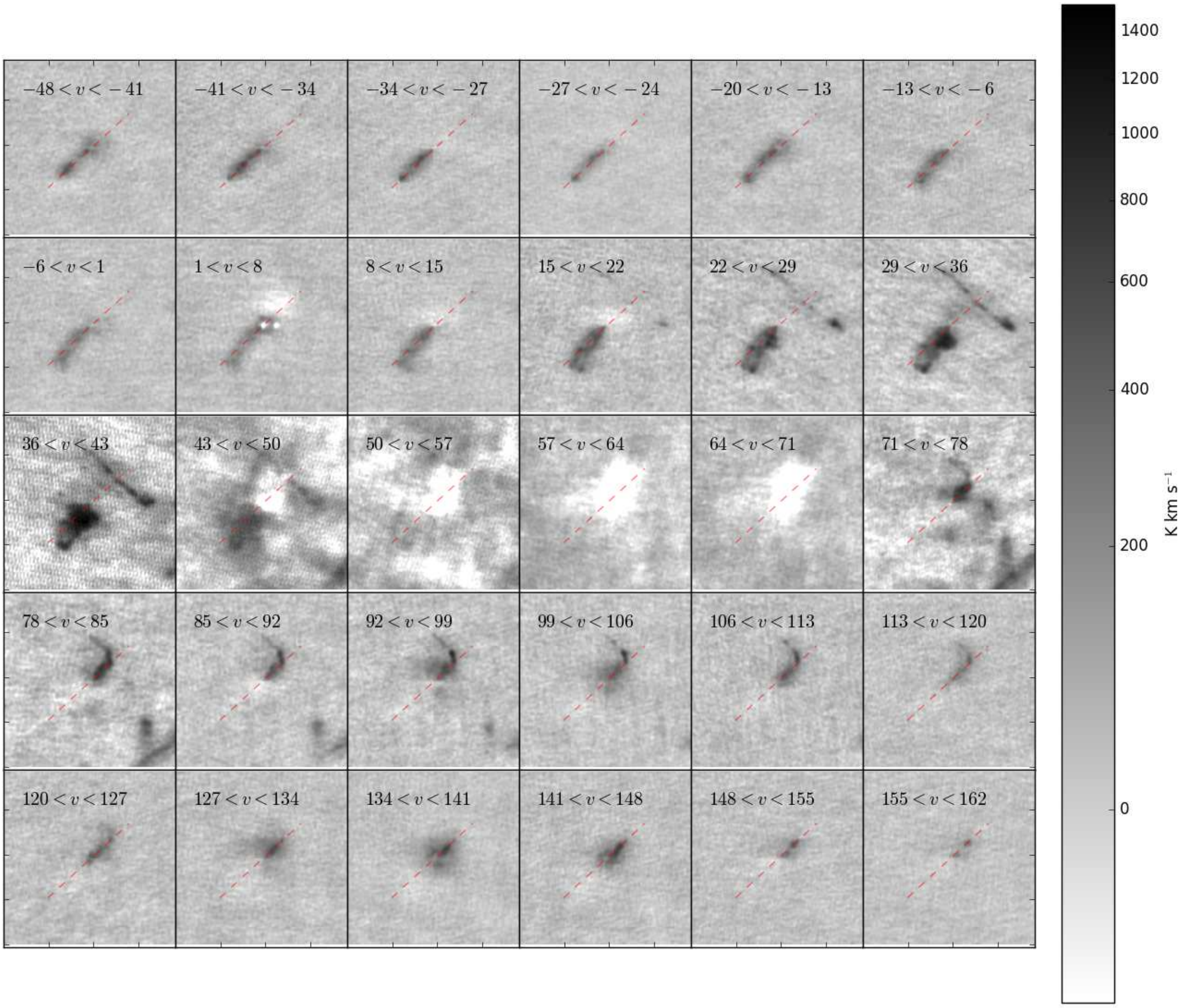

Fig. 23. Channel maps of the e2e outflow in CO 2-1. The dashed line approximately connects the northwest and southeast extrema of the flow.

For $Q_{\rm H} \sim 10^{49}$ s^{-1}, $\alpha_{\rm B} = 3 \times 10^{-13}\,{\rm cm}^3\,{\rm s}^{-1}$, $R_{\rm s} \approx 0.01\,{\rm pc}$.

The Spitzer solution for HII region expansion gives

$$R_{\rm HII}(t) = R_{\rm s}\left(1 + \frac{7}{4}\frac{c_{\rm II}t}{R_{\rm s}}\right)^{\frac{4}{7}}. \quad \text{(A.2)}$$

With $c_{\rm II} = 7.5\,{\rm km\,s^{-1}}$ and $t = 10^4\,{\rm yr}$, $R_{\rm HII}(t) \approx 0.04\,{\rm pc}$, while at $t = 10^5\,{\rm yr}$, it is $R_{\rm HII} \approx 0.16\,{\rm pc}$, which is comparable to the observed radius ($r_{obs} \sim 0.13 - 0.19$ pc)

Whitworth et al. 1994 give the fragmentation timescale as

$$t_{\rm frag} \sim 1.56\left(\frac{c_{\rm s}}{0.2{\rm km\,s^{-1}}}\right)^{\frac{7}{11}}\left(\frac{Q_{\rm H}}{10^{49}{\rm s^{-1}}}\right)^{-\frac{1}{11}}\left(\frac{n}{10^3{\rm cm^{-3}}}\right)^{-\frac{5}{11}} {\rm Myr} \quad \text{(A.3)}$$

Plugging in our numbers gives $t_{\rm frag} \approx 1.0 \times 10^5\,{\rm yr}$, or $10\times$ longer than the expansion time.

These values are consistent with a late O-type star having been exposed, driving an H II region, for $\sim 10^4 - 10^5$ year, after which a substantial increase in the accretion rate quenched the ionizing radiation from the star, trapping it into a hypercompact ($r < 0.005$ pc) configuration. The recombination timescale is short enough that the ionized gas would disappear almost immediately after the continuous ionizing radiation source was hidden. This is essentially the scenario laid out in **?** as an explanation for the compact H II region lifetime problem. In this case, however, it also seems that the H II region has effectively driven the "collect" phase of what will presumably end in a collect-and-collapse style triggering event.

Technically, it is possible that e5 actually represents an optically thick high-mass-loss-rate wind rather than an ultracompact HII region, but I think we can rule this out on physical plausibility considerations if we compare to wind models. Note that η Car would have a flux of ~ 0.5 Jy at 2 cm and ~ 5 Jy at 1 mm at the distance of W51.

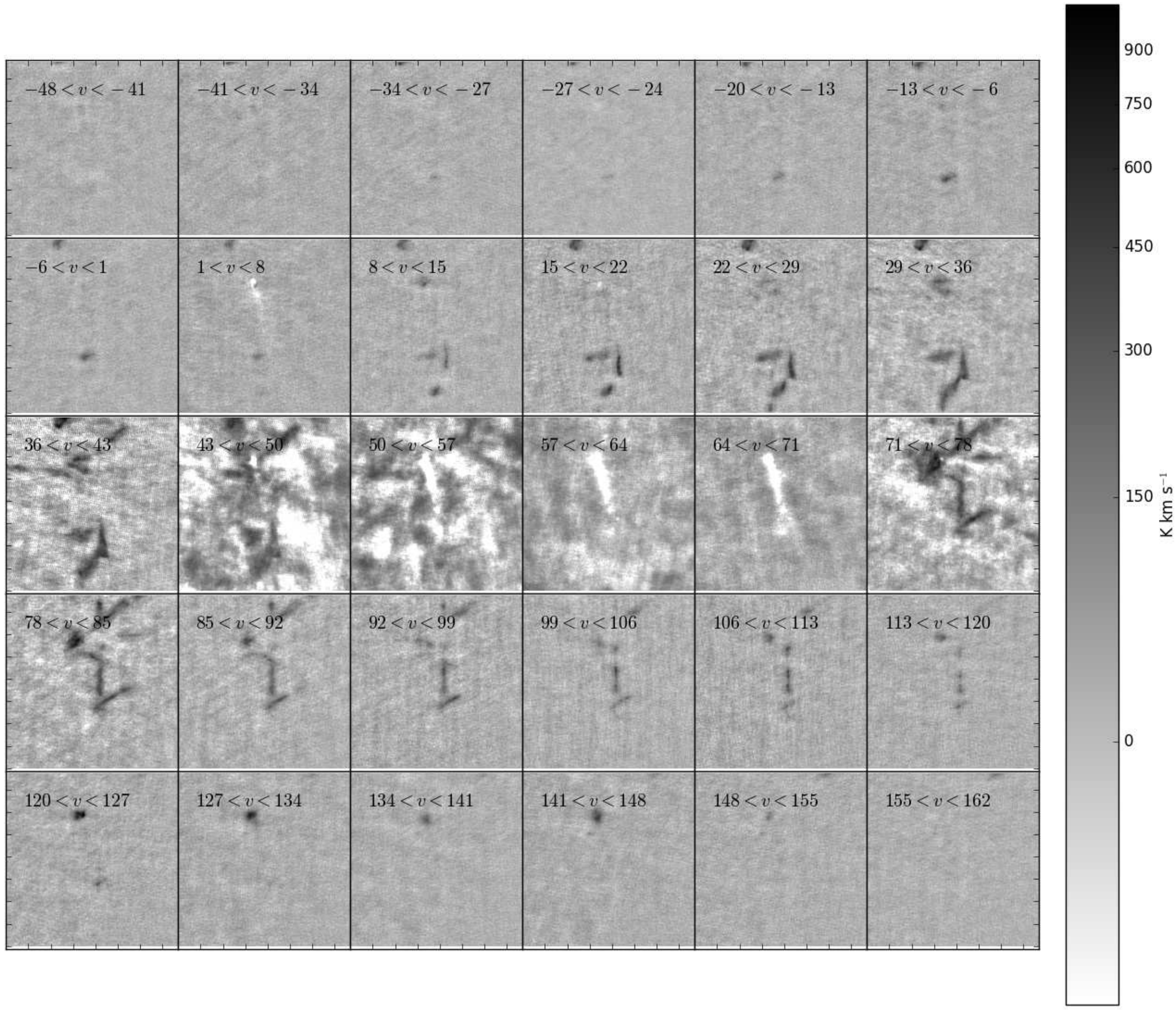

Fig. 24. channel maps of the e8 outflow in CO

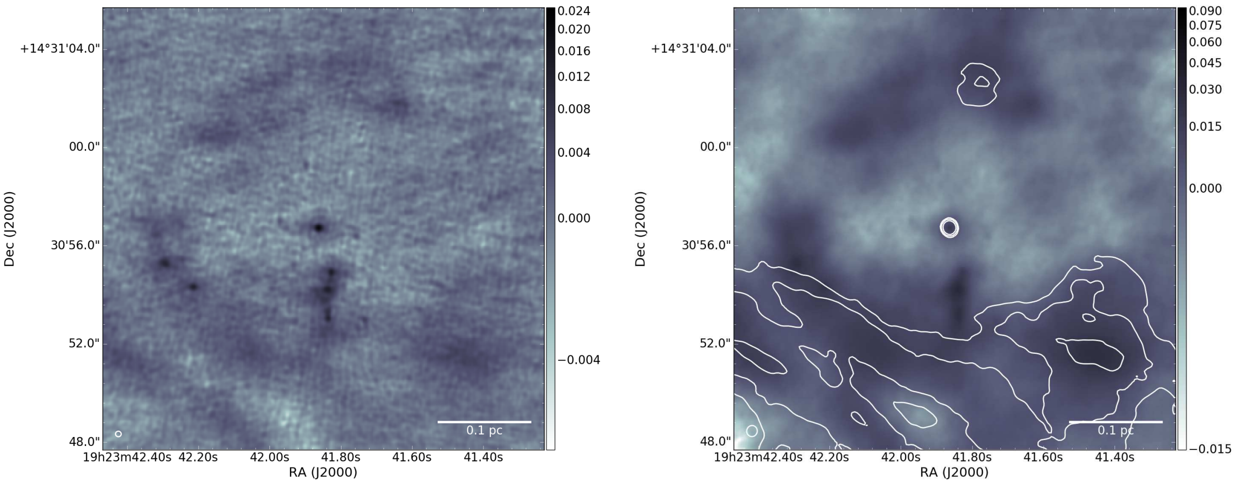

(a) (b)

Fig. A.1. The bubble around source e5. The bubble interior shows no sign of centimeter emission, though the lower-left region of the shell - just south of the "cores" - coincides with part of the W51 Main ionized shell. The source of the ionization is not obvious. (*Left*): A robust -2.0 image with a small ($0.2''$) beam and poor recovery of large angular scale emission. This image highlights the presence of protostellar cores on the left edge of the bubble and along a filament just south of the central source. (*Right*): A robust $+2.0$ image with a larger ($0.4''$) beam and better recovery of large angular scales. The contours show radio continuum (14.5 GHz) emission at 1.5, 3, and 6 mJy/beam. While some of the detected 1.4 mm emission in the south could be free-free emission, the eastern and northern parts of the shell show no emission down to the 50 μJy noise level of the Ku-band map, confirming that they consist only of dust emission.